Determining the Mechanical Properties of Rainbow Smelt (*Osmerus mordax*) Eye Tissue Using Atomic Force Microscopy (AFM)

by

©Lucas D. Stewart

A thesis submitted to the School of Graduate Studies in partial fulfillment of the requirements for the degree of

Master of Science

Department of Chemistry

Memorial University of Newfoundland

June 2016

St. John's Newfoundland

Abstract

Hyperosmotic stress is the condition of increased cellular osmotic pressure and is linked to a number of mammalian diseases. One such disease is diabetes mellitus, which is characterized by a state of elevated blood glucose concentration which eventually can lead to such issues as a leakage of fluids from the blood vessels into the surrounding eye tissue. The resulting increase in osmotic pressure of the eye can lead to the eventual vision loss which is seen in diabetic patients. Other examples of hyperosmotic condition exist in nature, one such case being found in Rainbow Smelt. In this case, smelt are capable of surviving in colder water environments by increasing the osmotic pressure of their bodily fluids, including within the eye. This increase in osmotic pressure depresses the freezing point of their bodily fluids, allowing for adaptation to colder climates. However, the fish's vision isn't impacted by the hyperosmotic state.

The object of this work is to study the key structural and mechanical properties of sections of rainbow smelt eye using Atomic Force Microscopy (AFM). Two subgroups of smelt were studied: ones raised in a warm water environment that show no hyperosmotic conditioning, and ones raised in a cold water environment which show elevated osmotic pressures in the eye. Comparisons between the two smelt subgroups were made in both dry and hydrated environments. By determining any key structural, mechanical, or chemical changes in the cold smelt eye, we hope to better understand the hyperosmotic conditioning that takes place within the eye.

Acknowledgements

First and foremost I would like to thank Dr. Erika Merschrod for giving me this opportunity to return back to her research group to complete my Masters of Science program. She has been an excellent mentor through all the years I've known her, and the way Erika is able to motivate her students to strive for their best is truly admirable. Due to this, there's no other group I'd rather study in. Erika, from the bottom of my heart, thank you for everything you've done for me.

I'd also like to thank the entire Merschrod research group for being an excellent group of individuals to work with. Special thanks to the "Bio sub-group" of Asia Alhasawi, Dong Zhe, Garrett McDougall, David Gale, and Ryan Wilkins for their helps with such a challenging project.

Special thanks go out to my closest group of MUN chemistry friends: Kerri, Teles, Doug, Josh, and Liam. You've kept me on track through some of the more trying times of this program. Last but not least, I'd like to thank my parents and girlfriend Kathleen, who have been extremely supportive throughout this whole time. Without you all, I wouldn't have been able to do this.

Table of Contents

List of Tables

List of Figures

List of Abbreviations and Mathematical Constants

AFM	Atomic Force Microscopy
SEM	Scanning Electron Microscopy
osmol	Osmolarity
K	Kelvin
N	Newton
nN	Nanonewton
pN	Piconewton
DLVO	Dejarguin-Landau-Verwey-Overbeck
DMT	Derjaguin-Muller-Toporov
OCT	Optimal cutting temperature
invOLS	Inverse optical lever sensitivity
MPa	Megapascals
GPa	Gigapascals
LC	Liquid chromatography
ESI/MS	Electrospray ionization mass spectrometry
TERS	Tip-enhanced Raman spectroscopy
PDMS	Polydimethylsiloxane

Π	Osmotic pressure
i	Van 't Hoff Factor
k_b	Boltzmann constant (1.3806×10^{-23} JK^{-1})
N_A	Avogadro's number (6.022×10^{23} mol^{-1})
T	Temperature of system
M	Molarity of solution
φ_i	Osmotic coefficient of solution
n_i	Number of ions in which the solute dissociates in to in solution
F	Force acting upon the AFM tip
k_c	Spring constant of the AFM tip
x	Cantilever deflection
m	Mass of AFM tip
F_0	Amplitude of the tip frequency
Q	Quality factor of AFM tip
ω	Angular frequency of the driving force
ω_0	Angular resonance frequency
$F_{t,s}$	Tip-sample interaction force
A	Hamaker constant
z_c	Tip-sample rest distance
Z	Instataneous tip-sample distance
ρ	Density of the fluid medium
b	Width of the AFM cantilever
Γ	Hydrodynamic function
$\hat{W}$	Fourier transform of the cantilever displacement
R	AFM tip radius
ϵ	Dielectric constant of the medium

ϵ_o	Permittivity of free space (8.854×10^{-12} Å^2 s^4 m^{-3} kg^{-1})
$\frac{1}{K_d}$	Debye length
σ_t	Surface charge on the AFM tip
σ_s	Surface charge on the sample
E'	Effective Young's Modulus
E_s	Young's Modulus of the sample
E_t	Young's Modulus of the tip
E^*	Reduced Young's Modulus
a_o	Intermolecular distance between two objects
EI	Flexural rigidity of AFM tip
p_c	Mass per unit length of AFM tip
$w(x,t)$	Transverse deflection of AFM tip
F_{hydro}	Hydrodynamic dampening force
F_d	Force driving the tip oscillation
L_c	Cantilever length
A_o	Area of applied force
ΔL	Extension length in the direction of the stress
L_o	Original length of sample
δ	Indentation depth of the sample
v_s	Poisson's ratio of the sample
v_t	Poisson's ratio of the tip
F_p	Force of adhesion
γ	Work of adhesion per unit area
π	pi (3.14159)
Δd	Jump-to-contact distance
γ_w	Surface tension of water

H	Relative humidity of the environment
λ_k	Kelvin length of water (0.523 nm at 25 °C)
S_o	Tip-sample separation

Chapter 1

Introduction

1.1 Hyperosmotic Condition

Homeostasis, or the process of maintaining stability within a system, is extremely important for all living organisms [1]. In the case of the mammalian body, homeostasis is required for many biological functions to occur properly, and any drift from an optimal environment could have adverse or lethal consequences. Factors such as pH [2], body temperature [3], blood glucose concentration [4], and cellular copper concentration [5] are maintained within their optimal ranges through various feedback loops within the body.

Along with the various properties listed above, another important physiological factor to consider is the tonicity of the cellular environment. In biophysics, the tonicity of a cell refers to the solute concentration difference between the interior of the cell and its external environment [1]. Depending on the solute concentrations within the system, there are three relationships that the environments can have with each other. Under ideal conditions, when the solute concentrations inside the cell are equal to that of the extracellular medium, then the environment is considered to be *isotonic*. In

this scenario, no concentration gradient exists between the two environments; water flows in and out of the cell at equal volumes resulting in no deformation to the cell structure, as illustrated in Figure 1.1.

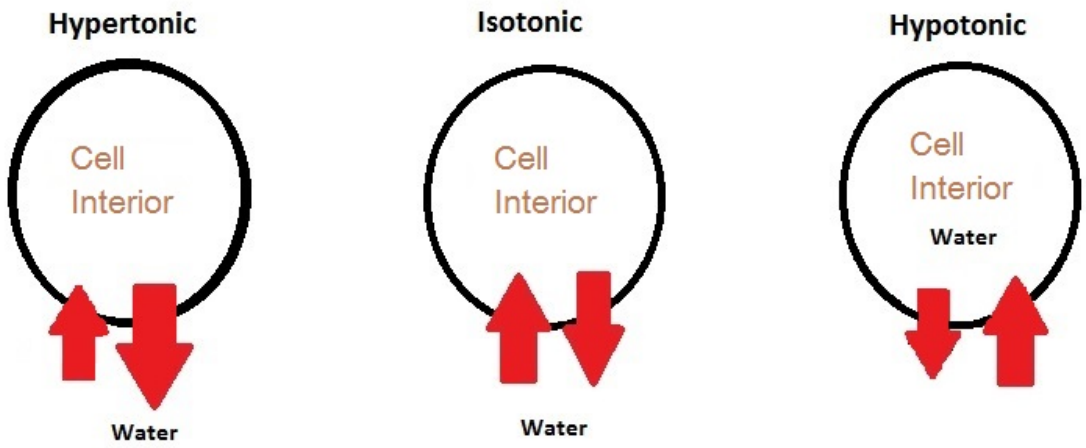

Figure 1.1: Schematic showing hypertonic (left), isotonic (centre), and hypotonic (right) conditions of a cell.

However, when the solute concentration outside the cell is larger than inside the cell, the extracellular solution is considered *hypertonic* [1]. Under these conditions, the concentration gradient between the cell interior and exterior results in a net flow of water out of the cell. The loss of water results in the cell to shrink in size, which can be seen in Figure 1.2. In comparison, when the solute concentration inside the cell is larger than its surroundings, the extracellular solution is considered *hypotonic*. Water from the surrounding environment enters the cell due to the concentration gradient, causing it to swell and possibly lyse (burst).

The relationship between a cell and its external environment can also be expressed using osmotic pressures [6]. The osmotic pressure is defined as the minimum pressure required to prevent the spontaneous inward flow of water from the environment into the cell. In an isotonic environment, the osmotic pressure of the solutions both inside and outside the cell are equal, allowing no net flow of water in the environment. When

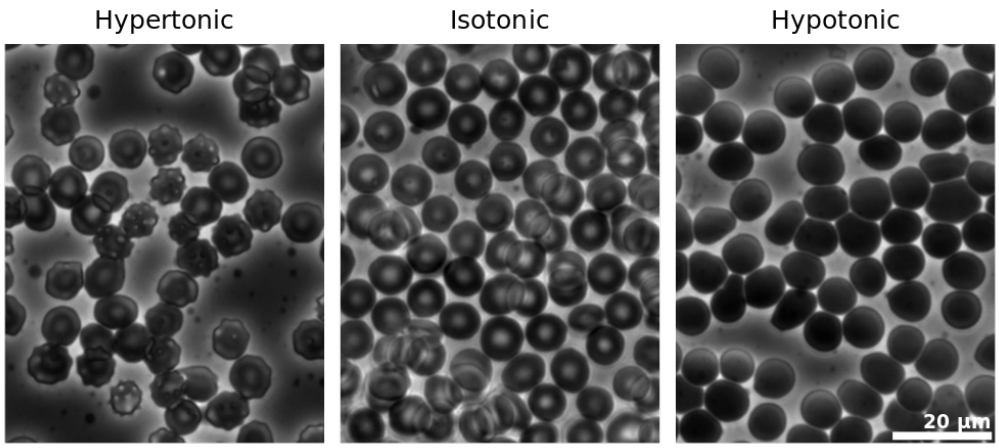

Figure 1.2: Scanning Electron Microscope (SEM) image showing red blood cells under hypertonic (left), isotonic (centre), and hypotonic (right) conditions. Public Domain (Wikimedia Commons, created by user Zephyrus)

the osmotic pressure outside the cell is larger than inside the cell, the extracellular environment is considered hypertonic, and water will flow into the cell. For a hypotonic solution, the osmotic pressure inside the cell is greater than its extracellular environment, causing a net flow of water out of the cell. To determine the osmotic pressure Π of a solution, the Morse equation can be used:

$$\Pi = iMN_A k_b T \tag{1.1}$$

where M is the molarity of the solution, N_A is Avogadro's Number (6.022×10^{23} mol^{-1}), k_b is the Boltzmann constant (1.3806×10^{-23} J K^{-1}), T is the temperature of the system, and i is the van 't Hoff Factor, a value describing the degree of dissociation of the solutes in solution. When working with osmotic pressures, often one describes concentrations using osmolarity over molarity. An osmole (abbreviated osmol) describes the total number of solutes which contribute to the overall osmotic pressure of the solution, and as such osmolarity can be defined as the number of osmoles per litre of solution (osmol/L) [6], and can be determined by the following equation:

$$\text{osmolarity} = \sum_i \varphi_i n_i M_i \tag{1.2}$$

where for solute i, M is the molar concentration, n is the number of ions in which the solute dissociates in to in the solution, and φ is the osmotic coefficient, which can be estimated as the degree of dissociation of the solute molecules.

In biophysics, it is common to describe cellular environments through the internal cell conditions as opposed to the external solution as described above. As such, a cell placed in a hypotonic external solution can easily be described based on its internal environment. In this case, the osmotic pressure inside the cell is greater than its extracellular environment, and hence the cell interior can be described as hypertonic or hyperosmotic. The same applies with a cell placed in a hypertonic solution; the osmotic pressure of the extracellular environment is higher than that of the intercellular environment, and the interior of the cell can be described as hypotonic or hypoosmotic. [7]

1.1.1 Diabetes Mellitus

Diabetes mellitus is a metabolic disease characterized by an increased state of blood glucose levels (hyperglycemia), which is a direct result of either improper insulin secretion from the pancreas or improper insulin action within the body [8]. Diabetes mellitus, commonly just called diabetes, is widely growing across the world, with an estimated 381.8 million people between the ages of 20 and 70 having the disease, a number which is estimated to grow to 591.1 million by the year 2030 [9].

There are two main types of diabetes: type 1 and type 2. Type 1 diabetes is prevalent in only 3–4% of the population which suffer from the disease [10], and is characterized by the destruction of pancreatic β-cells by the immune system [8].

Table 1.1: Statistics showing the number of diabetes mellitus cases worldwide in 2013 as published in Diabetes Research and Clinical Practice [9]

Region	People with diabetes (aged 20-79) in millions	National prevalence in population (aged 20-79) (% of population)
Africa	19.8	4.9
Europe	56.3	8.5
Middle East & North Africa	34.6	10.0
North America & the Caribbean	36.7	11.0
South & Central America	24.1	8.0
South-East Asia	72.1	8.2
Western Pacific	138.2	8.6
Worldwide	381.8	8.3

Without the functioning β-cells to produce the insulin peptide, excess glucose in the blood stream is not removed, resulting in hyperglycemia. In comparison, type 2 diabetes is characterized by an insulin resistance or insulin deficiency within the body, and accounts for most of the other diagnosis [8]. Upon initial screening, insulin levels in the body may appear normal, however the inability for the β-cells of the pancreas to produce higher amounts of insulin to compensate for increased blood glucose concentrations is a tell-tale sign of type 2 diabetes.

The dangers of uncontrolled blood glucose concentrations are well understood, and includes damage of vital organs such as the kidneys, heart, and nervous system [8]. Another huge consequence of diabetes is the risk of diabetic retinopathy, a disease characterized by an increase in leakage of retinal blood vessels into its surroundings, resulting in a lack of blood supply to the retina (retinal ischemia) [11], which can be seen in Figure 1.4.

Leakage from retinal blood vessels can lead to a complication in the eye called macular edema, where the retina and macula swell and harden, resulting in impaired vision and eventual vision loss [13, 14]. The process of blood vessel leakage and subsequent cellular swelling is caused by the hyperglycemic state of blood within the

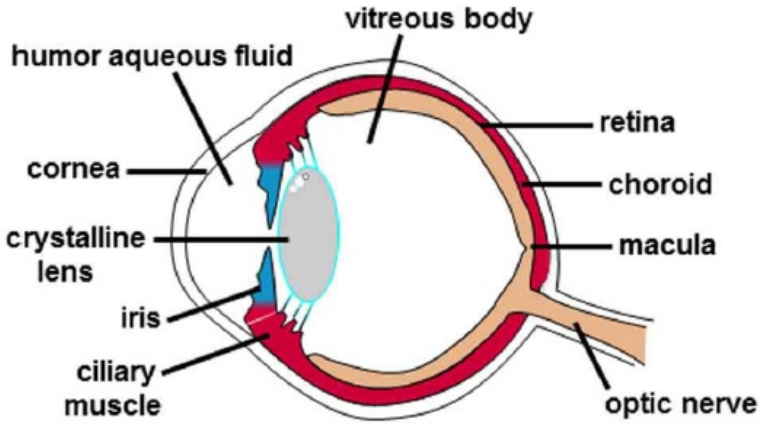

Figure 1.3: The structure of the human eye [12]

vessels, resulting in physical and chemical changes of the vessels, ultimately leading to a blood-retinal barrier breakdown.

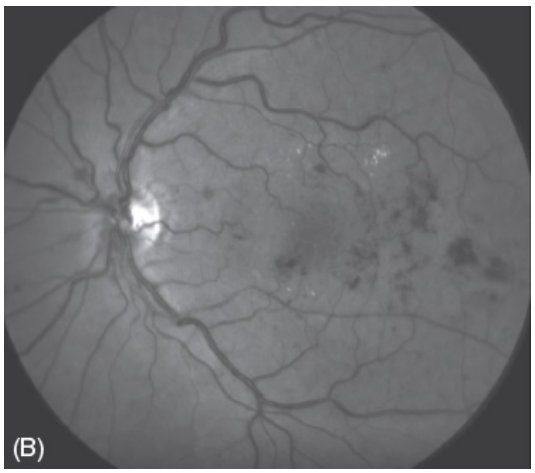

Figure 1.4: Angiogram of a human eye showing the leakage from the blood vessels (circular pools of fluid on far left of image) [15]

Due to the continued hyperglycemic state of the blood in diabetic patients, diabetes is considered a hyperosmotic disease [7]. Hyperglycemia of the blood results in higher concentrations of glucose within the cells of the retina, which in turn causes an increase intrecellular sorbitol levels [14]. This, along with the leakage of proteins

and fluids into the retina from the blood-retina barrier breakdown, results in an overall increase in osmotic pressure of the retina [12], as predicted by equation 1.1. In addition to other complications related to diabetes [16], the increase in cellular osmotic pressure causes water to flow freely into the cells from the extracellular matrix, swelling, and resulting in eventual vision loss [14].

1.1.2 Rainbow Smelt and Hyperosmotic Conditions

As seen in Section 1.1.1, hyperosmotic stress can have a profound effect on ones health, and can lead to issues such as vision loss in diabetic patients. There are other examples of hyperosmotic condition existing in nature, one of which being in the teleost subclass of fish [17]. Under normal conditions, the expected bodily fluids freezing point in teleosts is approximately -0.65 °C. However in locations such as the North Atlantic ocean, water temperatures in the winter months often reach below -1.0 °C [18]. In response, teleost fish have a cysteine-rich antifreeze protein which helps reduce the freezing point of their fluids, however they are also unique in that they have higher levels of glycerol, urea, and trimethylamine oxide in their body [19]. These compounds increase the osmotic pressure of the teleost bodily fluids to a near isosmotic state with the surrounding seawater, depressing the freezing point, and thus adapting to the cold water environment without freezing.

Research performed by Robert Gendron [19] specifically studied the rainbow smelt (*Osmerus mordax*) subspecies of telost, which are common to the waters of the North Atlantic ocean. The smelt were collected and split into two sub-groups: the first were placed in a tank held at a constant "warm" water temperature of 8–10 °C, and the others were placed in a tank that where water temperature tracked the ambient temperature of the North Atlantic ocean, where during the winter months the temperature would drop below a "cold" 0.5 °C.

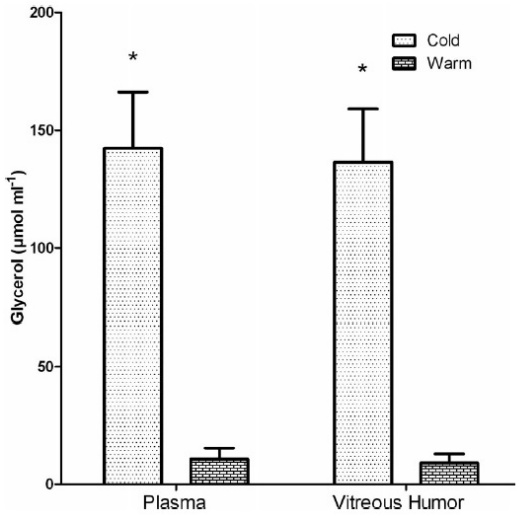

Figure 1.5: The glycerol concentrations of the rainbow smelt blood plasma and vitreous humor, showing the difference between the fish raised in warm and cold water environments [19]

Analysis of both the smelt blood plasma and vitreous humor (fluid of the eye) was performed to determine their glycerol levels and osmotic pressures. As seen in Figure 1.5, elevated glycerol concentrations are present in both the blood plasma and vitreous humor of the fish raised in the cold water environment. This result is consistent with previous studies performed on blood plasma of rainbow smelt [17], however this was the first report of glycerol accumulation in the vitreous humor of a telost fish.

Elevated glycerol levels in the cold environment rainbow smelt directly correlated with an increase in osmotic pressure of the vitreous humour as seen in Figure 1.6 [19]. Based on the osmotic pressures, the freezing points for the cold and warm smelt vitreous fluids were calculated as -1.20 ± 0.9 °C and -0.62 ± 0.03 °C respectively. This freezing point depression in the cold water fish is sufficient enough to prevent bodily fluids from freezing during the cold winter months. Hence we can conclude that rainbow smelt have a hyperosmotic adaptation in which they prevent freezing during the winter months by accumulating glyerol and other osmolytes to increase the osmotic

pressure of their bodily fluids, including in their eyes. However, very little is known on how the structure or physical properties of the smelt eye may be affected by the hyperosmotic conditioning.

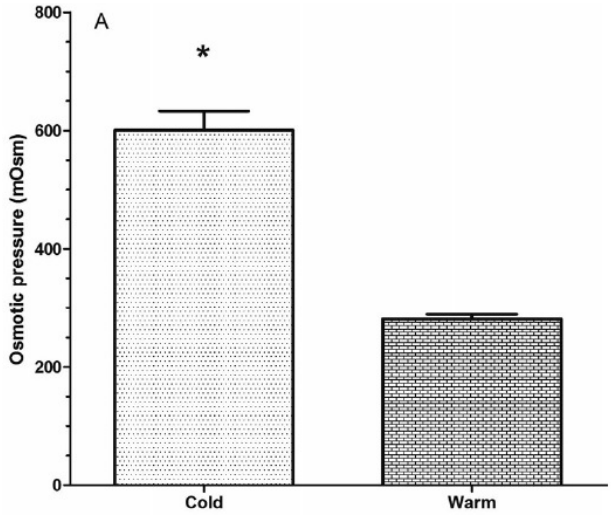

Figure 1.6: Osmotic pressure of the vitreous humour fluid of rainbow smelt raised in both warm and cold water environments [19]

1.2 Atomic Force Microscopy

Atomic Force Microscopy (AFM) is a scanning probe method which can be used to gather mechanical and topographical information of many types of materials, and, under the ideal conditions, is able to achieve atomic resolution [20]. In simplest terms, AFM works by monitoring the interactions between an AFM tip (with a radius typically between 10–50 nm) and the sample being studied. Highly sensitive electronics within the instrument monitor this tip-sample interaction, the results of which produces a topographic image. A more in depth explanation of how each type of AFM imaging will be given in Sections 1.2.1 and 1.2.2.

Figure 1.7 shows the set up for a typical AFM experiment. A cantilever with a tip is loaded into the cantilever holder and a laser is then aligned onto the back of the tip. This laser is directed off the back of the tip into a photodiode array which compiles the laser deflection data and sends it to the detector. Movement during the scan is controlled through a piezoelectric actuator (labelled PZT in Figure 1.7), which moves the sample during the scan. A raster scan is performed during the experiment, in which the AFM tip scans along the surface in one direction (x), collects data, and then returns back to the point of origin of the scan [21]. From here, the sample is moved a pre-determined distance in the (y) direction, and another scan across the sample is performed. The spacing between each line in the (y) direction and the number of data points taken per line in the (x) direction determines the resolution of the final AFM image: the more data collected and the smaller spacing between each scan line will result in a more data-rich scan, and ultimately higher resolution.

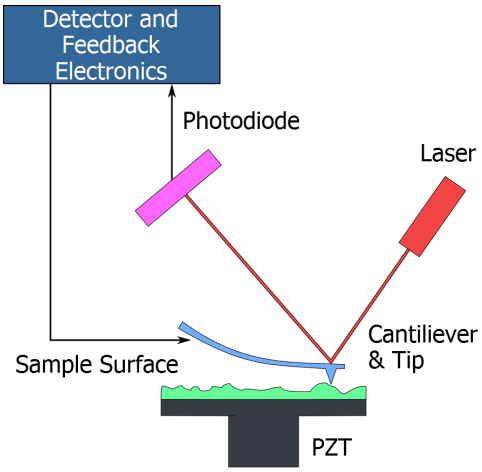

Figure 1.7: Block diagram depicting a typical AFM experimental setup. Public Domain (Wikimedia Commons, created by user OverlordQ)

To understand how the AFM feedback loop works, an understanding of the relationship between the laser and the photodiode is needed. As the AFM tip scans

across the sample, various tip-sample forces such as electrostatics [22] and van der Waals [23] interactions will result in the tip being bent and twisted from its original resting position. This results in the laser path from the back of the tip to the photodiode being altered. The photodiode array itself is composed of four equally-sized segments, commonly labelled A, B, C, and D to distinguish their position, as seen in Figure 1.8.

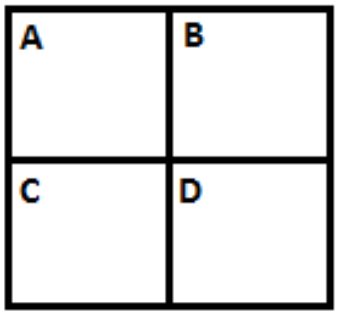

Figure 1.8: Schematic of a typical photodiode array used in AFM

The deflection value of the laser is determined by monitoring the laser intensity in each quadrant of the photodiode, and can be expressed mathematically using the following equation:

$$\text{Deflection} = (A + B) - (C + D) \tag{1.3}$$

where the values of A, B, C, and D are the respective laser intensity in each quadrant. Before each experiment, the photodiode can be moved to set the total deflection value to a desired set point for the scan. As the tip scans along the sample surface, the bending of the AFM tip will cause the deflection value at the photodiode array to change from the initial set value, and this information is then sent to the built-in

feedback loop. This mechanism is the basis behind contact mode AFM, a standard topographic method used to image samples, which will be further outlined in 1.2.1.

1.2.1 Contact Mode AFM

Contact mode AFM is the most basic of AFM imaging techniques and was published by Binnig *et. al.* in their paper proposing the new scanning probe method [24]. As the AFM tip is brought towards the surface of the sample, van der Waals and electrostatic forces act upon the tip as seen in Figure 1.9. Initially electrostatics and van der Waals forces between the tip and the sample are net attractive, however as the tip-sample separation decreases the net force between the two becomes repulsive. This net repulsion is caused by the Born repulsion due to the electronic orbital overlap of the tip and the sample [25].

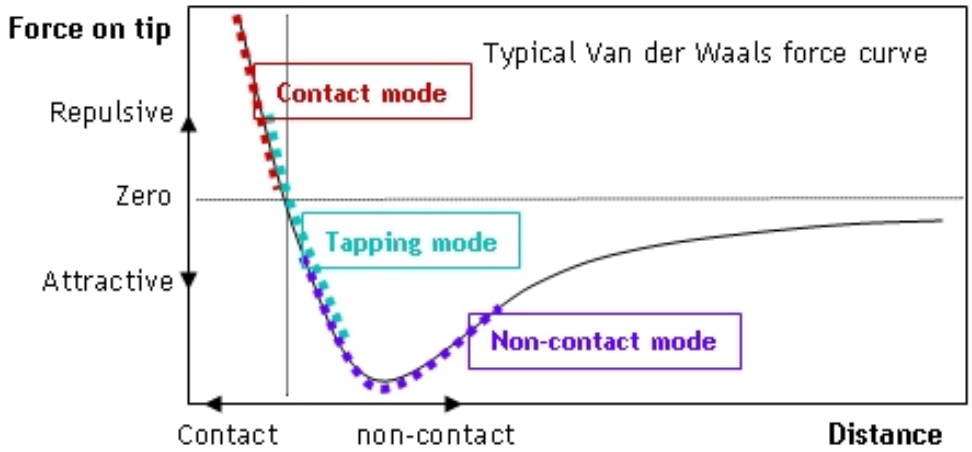

Figure 1.9: Force-distance curve showing the net force on the AFM tip in each imaging mode. Public Domain (Wikimedia Commons, created by user KristinMolhave)

As the tip comes in contact with the sample, the overall net repulsive force on the tip is on the magnitude of 10^{-9} to 10^{-10} N [26]. The force acting upon the tip can be related to the laser deflection through Hooke's Law:

$$F = -k_c x \tag{1.4}$$

where F is the force acting on the tip, x is the cantilever deflection value, and k_c is the spring constant of the AFM tip (typically on the order of magnitude of 0.1 N/m). The desired force during the scan can be input as a set point value prior to bringing the tip into contact with the surface, and can be changed in between scans if desired.

The feedback loop for contact mode imaging is dependent on keeping the force acting on the tip constant, which is monitored through the cantilever laser deflection as seen in equation 1.4 [24]. As the tip scans across the surface, variations in height of the sample will result in a change in the repulsion force felt by the tip. These changes correspond with a change in the cantilever laser deflection value, as changes in the forces felt by the tip will result in the tip bending, changing the incident angle of the laser reflecting off the cantilever to the photodiode array. The change in laser deflection (and hence force) will alert the feedback electronics in the AFM that the value has drifted from the set point, resulting in a voltage being applied to the z-axis piezoelement to move the sample (or tip, depending on the AFM instrument) up or down to restore the laser deflection back to the original set point. This applied voltage is what determines the height profile of the surface, and the output is a typical AFM topography image.

1.2.2 Tapping Mode AFM

Tapping mode AFM, also known as amplitude-modulated AFM, is a method of AFM imaging that does not rely on the tip being in constant contact with the sample as seen in contact mode imaging. In tapping mode, the tip is resonated at (or more often near) its resonance frequency, and results in the tip making periodic contact, or

"tapping" the surface being scanned [27]. The reduction in tip-sample contact time during a topographic scan is highly advantageous due to the reduction of lateral force felt by the tip, which will help reduce sample destruction and unwanted image artifacts during scanning [28]. The feedback loop for tapping mode monitors the amplitude of the tip frequency as the tip scans the surface. An initial amplitude value is set in much the same way the force set point is used in contact mode imaging, however in tapping mode imaging the laser deflection is not used in the feedback loop. As the tip scans the surface, height variations will result in a dampening of the tip frequency, resulting in a change of its amplitude compared to the initial set point. As the same in contact mode AFM, voltage is applied to the z-axis piezoelement to move the sample (or tip) up or down to restore the set amplitude [27].

García and Paulo [29] describe the motion of an AFM cantilever during a tapping mode scan as a combination of tip-sample interaction (dominantly attractive as seen in Figure 1.9), the tip excitation force, hydrodynamic damping of the tip in the medium, and the elastic response of the tip. An equation to describe this was given as follows:

$$m\frac{dz^2}{d^2t} = -k_c z - \frac{m\omega_0}{Q}\frac{dz}{dt} + F_{t,s} + F_0 cos\omega t \tag{1.5}$$

where F_0 is the amplitude of the tip frequency, ω is the angular frequency of the driving force, $F_{t,s}$ is the net-attractive force between the sample and the tip, ω_0 is the angular resonance frequency, Q is the quality factor of the tip, and k_c is the spring constant of the tip.

In particular, the tip-sample interaction ($F_{t,s}$) in equation 1.5 can be estimated mathematically. Assuming the AFM tip as a sphere and the sample as flat surface [29], the tip-sample force can be estimated as:

$$F_{t,s}(z_c, z) = -\frac{AR}{6(z_c + z)^2} \tag{1.6}$$

where A is the Hamaker constant, R is the tip radius, z_c is tip-sample rest distance, and z is the instantaneous tip-sample distance, which is illustrated in Figure 1.10.

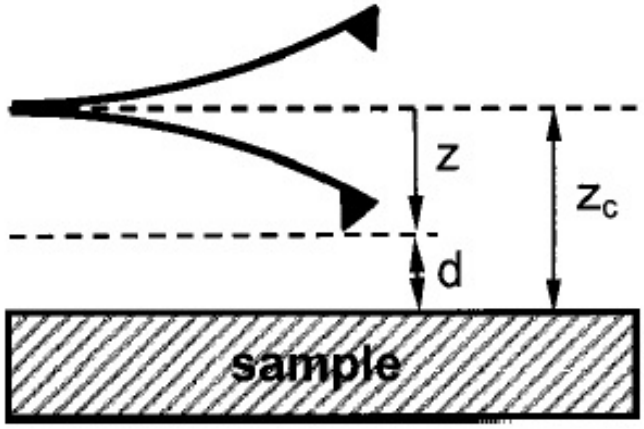

Figure 1.10: AFM tip operating in tapping mode, showing the tip-sample distance at rest (z_c) and while oscillating (z) [29]

Tapping mode imaging is especially advantageous over traditional contact mode when working with delicate biological samples. In standard contact mode, a continuous force is being applied to the sample from the tip during scanning, which can lead to sample destruction on particularly soft biological samples. Tapping mode allows for the collection of the same topographical information of the sample, but with minimal tip-sample contact, greatly reducing the chances of sample destruction during imaging [29].

1.2.3 AFM Imaging in Fluid

Many AFM instruments are capable of producing high resolution topographic images of samples in liquid environments along with the before-mentioned in-air methods [30].

This is highly advantageous in the field of biology, as being able to image in fluid allows for studies of proteins [31], individual cells [32], and tissues [33] in a more natural aqueous environment. Both contact and tapping modes can be used for imaging in fluid, however the disadvantages of contact mode imaging (e.g., possible sample destruction) make it less desirable to use than tapping mode.

When moving from tapping mode imaging in air to fluid, there are a number of physical factors which must be considered. As the tip oscillates in a fluid medium, the hydrodynamics of the cantilever will differ significantly than of that in air. As well, coupling of the oscillations with the low Reynolds number environment during the scan results in a lowering of the tips resonance frequency and quality factor (Q in equation 1.5) [34].

While little is still known about the dynamics of tips in liquid environments, two primary considerations have been identified by Baró and Reifenberger in their published book titled *Atomic Force Microscopy in Liquid: Biological Applications* [34]. The first of these is the hydrodynamics of an oscillating cantilever in a liquid environment. Under these conditions, oscillation of the AFM tip in a fluid medium introduces an additional force acting upon the tip, known as the hydrodynamic load per unit length, and can be calculated as [35]:

$$\hat{F}_{hydro}(x,\omega) = \frac{\pi}{4}\rho\omega^2 b^2 \Gamma(\omega)\hat{W}(x,\omega) \tag{1.7}$$

where ρ is the density of the fluid medium, ω is the driving frequency of the AFM tip, b is the cantilever width, $\hat{W}$ is fourier transform of the cantilever displacement at position x.

The other factor to consider when imaging in fluid is the tip-sample interactions which can be broken down into two parts: the tip-sample interaction when the tip is near the surface, and the tip-sample interaction when in contact with the surface.

Tip-sample interaction before contact is modelled using Derjaguin–Landau–Verwey–Overbeck (DLVO) theory [36]:

$$F_{ts}(d) = F_{DLVO}(d) = \frac{4\pi R}{\epsilon\epsilon_o K_d}\sigma_t\sigma_s e^{-K_d t} - \frac{AR}{6z^2} \tag{1.8}$$

where A is the Hamaker constant, R is the AFM tip radius, z is the instantaneous tip-sample separation distance, $\frac{1}{K_d}$ is the Debye length, ϵ is Dielectric constant of the medium (e.g., water), ϵ_o is the permittivity of free space $(8.854\times10^{-12}\mathrm{A^2s^4m^{-3}kg^{-1}})$, σ_t is the surface charge of the AFM tip, and σ_s is the surface charge of the sample. In contract, tip-sample interaction during contact can be modelled using Derjaguin-Muller-Toporov (DMT) theory [36]:

$$F_{ts}(d) = F_{DMT}(d) = \frac{4E'\sqrt{R}}{3}(a_o - z)^{\frac{3}{2}} + F_{DLVO}(a_o) \tag{1.9}$$

where E' is the effective Young's Modulus of the sample, a_o is the intermolecular distance, and $F_{DLVO}(a_o)$ is the solution to equation 1.8 at a tip-sample separation equal to a_o.

Basak and Raman [36] proposed a unifying model for describing the dynamics of an oscillating AFM tip in a viscous, polar liquid, and tapping on an elastic surface as:

$$EI\frac{d^4w(x,t)}{dx^4} + p_c\frac{d^2w(x,t)}{dx^2} = F_{hydro} + F_d + F_{ts}(Z_c - w(L_c,t)) \tag{1.10}$$

where EI is the flexural rigidity of the tip, which is a measure of the resistance of the tip while undergoing bending, p_c is the mass per unit length of the tip, $w(x,t)$ being the tranverse deflection of the tip, F_{hydro} is the hydrodynamic dampening force seen in equation 1.7, F_d is the force driving the tip oscillation, Z_c is the tip-sample rest distance seen in Figure 1.10, F_{ts} is the tip-sample force as seen in equations 1.8 and 1.9, and L is the cantilever length.

1.3 Force Spectroscopy

Shortly after the advent of AFM imaging techniques, the potential applications of the instrument began to come to light. One such application was the ability to investigate the molecular forces between the AFM tip acting as a sensor, and the sample being studied [37]. This new method, named "force spectroscopy", is capable of detecting forces in the range of piconewtons (pN) to nanonewtons (nN) in experiments that typically only take a few seconds to complete [37]. The range of forces that the AFM can sense is particularly useful in biological applications as it is capable of detecting the stronger covalent and electrostatic bonds between single molecules (nN range) [38] as well as antibody-antigen interaction (pN range) [39].

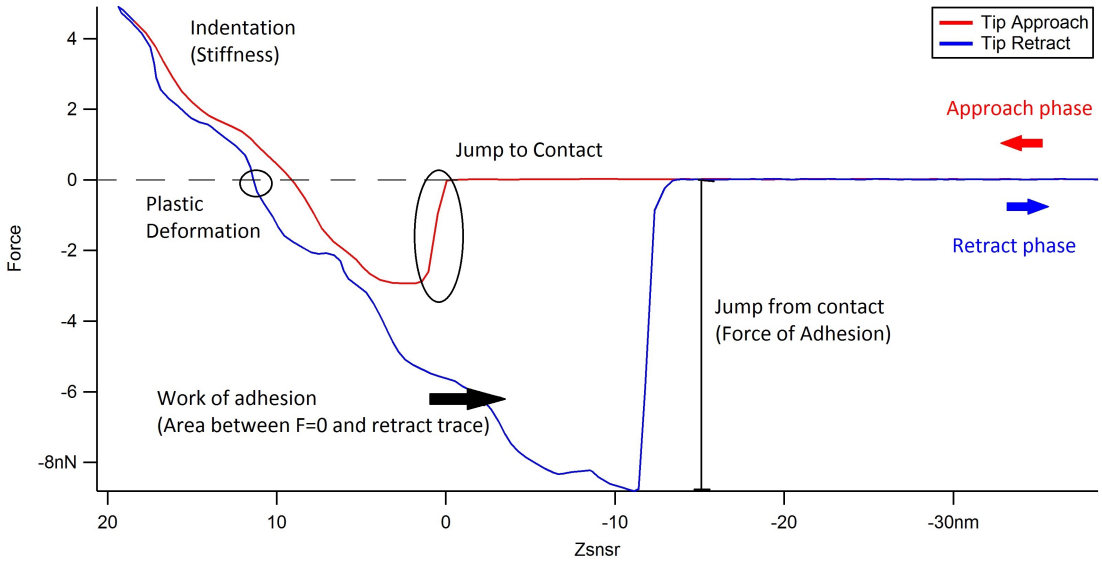

Figure 1.11: Typical force-distance curve showing the approach and retract phase, jump-to-contact, tip-sample adhesion, work of adhesion, plastic deformation, and indentation of sample.

In a typical force spectroscopy experiment, an AFM tip is held at a constant x and y position above the surface of the sample, and slowly begins moving towards the sample in the z direction. At this point, the laser deflection is constant as the

tip is left undisturbed. The approach of the tip towards the surface is represented along the x-axis of the force-indentation curve, such as the one in Figure 1.11. The "Zsnsr" represents the displacement between the sample surface resting position of the AFM tip as a force-distance curve is taken. As the tip approaches the sample, van der Waals and electrostatic attractive forces begin to be felt between the tip and sample [40]. These attractive forces continue to increase as the tip moves closer towards the sample. If the AFM tip is relatively soft (low spring constant), the attractive forces may eventually overcome the tip resulting in the tip jumping to contact with the sample, as seen in Figure 1.11. The tip continues to move towards the sample in the z direction and begins indenting into sample until a pre-determined indentation force has been reached. The applied force is controlled the same way as in contact mode imaging (Section 1.2.1) where the force applied to the sample by the tip is directly correlated to the laser deflection as seen in equation 1.4. Once the desired indentation force has been reached, the z piezo element begins to move the tip away from the sample surface, and is indicated by a new phase in the force-distance curve, shown as the blue trace in Figure 1.11. The tip continues to retract from the sample past the point of the initial jump to contact, where considerable tip-adhesion can be seen [40]. Eventually the AFM tip will retract to the point where the adhesion force is lesser than that of the tip stiffness, and the sample will jump from contact resulting in the tip returning to its rest position.

The resulting force-distance curve (often just called force curve) are rich in data, and can be used to determine a number of experimental parameters such as jump-to-contact distance of the tip and sample, the force of adhesion between the tip and sample (from the jump-from-contact). The degree of plastic deformation of the sample can also be determined from the presence of a hysteresis in the trace and retrace curves, where any hysteresis is indicative of the sample having some degree of

plasticity [41] or viscoelasticity [40]. The work of adhesion can also be determined by getting the area between the F=0 line and the retract curve [41]. One of the most useful areas of a force curve is the indentation phase, where key information about the stiffness of the sample can be extracted.

1.3.1 Determining the Young's Modulus from Force Spectroscopy

The elastic modulus, or Young's modulus, is a mechanical property of a object which is of great importance in biomaterials research. Knowing the Young's modulus of a cell or tissue is very important and can be useful in designing artificial biomaterials [42], diagnosing disease [43], or comparing healthy and diseased tissues [44].

The Young's modulus of a sample can be defined as the ratio of applied tensile stress to the tensile relaxation strain on the sample, and can be mathematically described as [45]:

$$E_s = \frac{\text{Stress}}{\text{Strain}} = \frac{\frac{F}{A_o}}{\frac{\Delta L}{L_o}} \tag{1.11}$$

where F is the force applied to the sample, A_o is the area of the applied force, ΔL is the extension length in the direction of the stress of the sample, and L_o is the original length of the sample. As stress has units of force per area and strain is a unit-less ratio, Young's modulus is recorded as a pressure, either in pascals (Pa) or pounds per square inch (psi) [45].

The Young's modulus of a sample can be indirectly determined from its force curve, and can be calculated using a number of different methods. These methods can be broken down into two different classes of contact mechanics: adhesive and non-adhesive analysis, both of which are discussed in further detail below.

1.3.1.1 Hertz Model

The Hertz model of contact mechanics was first introduced by Heinrich Hertz in 1882 as a way to describe how an applied force results in sample indentation between a sphere and flat surface in contact with each other [46]. The relationship between the applied force and sample indentation for a spherical indenter was given as [47]:

$$F = \frac{4}{3} E^* R^{\frac{1}{2}} \delta^{\frac{3}{2}} \tag{1.12}$$

where F is the applied force to the sample, R is the radius of the indenter, and δ is the indentation depth of the sample. E^* is the reduced Young's modulus, which can be determined by:

$$\frac{1}{E^*} = \frac{1 - \nu_s^2}{E_s} + \frac{1 - \nu_t^2}{E_t} \tag{1.13}$$

where E_s and E_t are the Young's modulus of the sample and of the indenter, respectively. ν_s and ν_t are the Poisson's ratios of the sample and tip, which is ratio of lateral to axial strain on a sample during indentation, and is often a value between 0.2 and 0.5 [48]. As the Young's modulus of the indenter (e.g., a silicon nitride AFM tip) is much larger than the Young's modulus of the sample, equation 1.13 can be simplified to:

$$\frac{1}{E^*} = \frac{1 - \nu_s^2}{E_s} \tag{1.14}$$

Combining equations 1.12 and 1.14 and rearranging yields an expression for the Young's modulus of the sample:

$$E_s = \frac{3}{4} F (1 - \nu s^2) R^{-\frac{1}{2}} \delta^{-\frac{3}{2}} \tag{1.15}$$

Equation 1.15 shows an expression relating the Young's modulus of a sample to the applied force and sample indentation, both of which can easily be determined from a force curve during a force spectroscopy experiment [49]. Many AFM analysis softwares allow simple conversion between force-distance to force-indentation curves like the one seen in Figure 1.12, which provides the force and indentation data needed to determine the sample Young's modulus.

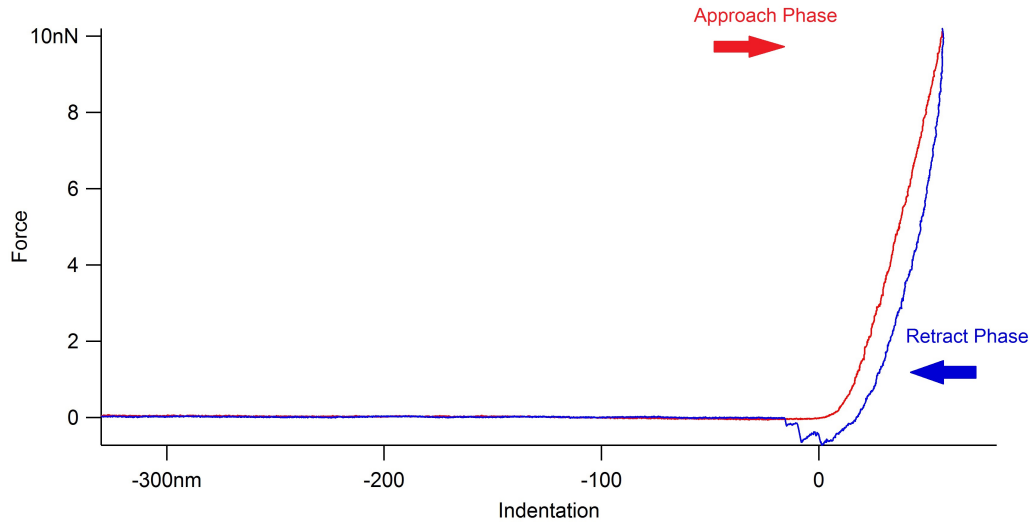

Figure 1.12: Force-indentation curve

While the Hertz model works well, is well understood, and is frequently used for analyzing force-distance curves, there are a few model assumptions which make its use for biological sample analysis not ideal. The first assumption is that the Hertz model assumes that the samples being investigated are purely elastic in nature [50]. While this may be true for many types of samples, biological samples often show significant viscoelastic behaviour [51, 52]. As well, the Hertz model falls under a "non-adhesive" analysis method as it assumes that there is no tip-sample interaction during the force experiment [53]. However, it can be seen from Figure 1.11 that many force curves show considerable tip-sample adhesion, and is especially common in experiments where biological samples are being probed. Ignoring these assumptions

during the analysis of biological force spectroscopy data is ill advised as they have a large contribution towards their mechanical properties. When analyzing in-air force curves, it is advisable to consider using models which take into consideration some of these factors.

1.3.1.2 Johnson–Kendall–Roberts Model and Minimal Indentation JKR

In 1971, Johnson, Kendall, and Roberts published the Johnson–Kendall–Roberts (JKR) model of contact mechanics which takes into consideration the adhesive forces between an indenter and sample [54]. The JKR model states that contact between two elastic objects under an applied force will result in a larger contact radius (a_1) than predicted from Hertz contact mechanics (a_0) due to adhesion between the two objects (see Figure 1.13). They also noted that along with these adhesive forces, tensile forces were present near the edge of the contact radius, all of which result in a higher applied force than what is accounted for in the Hertz model.

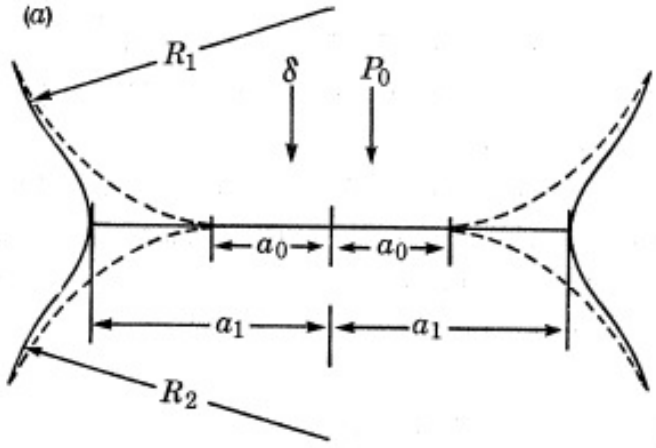

Figure 1.13: Contact between two elastic solids of radii R_1 and R_2 under an applied load P_0. Contact radius a_0 is the predicted contact radius under normal Hertz contact theory, whereas a_1 is the predicted radius contact under the JKR model [54]

Johnson *et. al* also gave an equation to quantify the adhesion force between the two elastic objects as:

$$F_p = -\frac{3}{2}\pi\gamma R \tag{1.16}$$

where γ is the work of adhesion per unit area, and R describes the radius of the two objects in contact, and is equal to:

$$R = \frac{R_1 R_2}{R_1 + R_2} \tag{1.17}$$

The JKR model of contact mechanics has recently been applied directly to force spectroscopy for determining the Young's modulus of samples. One such analysis method was described by D. Ebenstein, called the "two-point JKR" analysis method, calculates the reduced Young's modulus of the sample using only two points from a force curve as seen in Figure 1.14 [55].

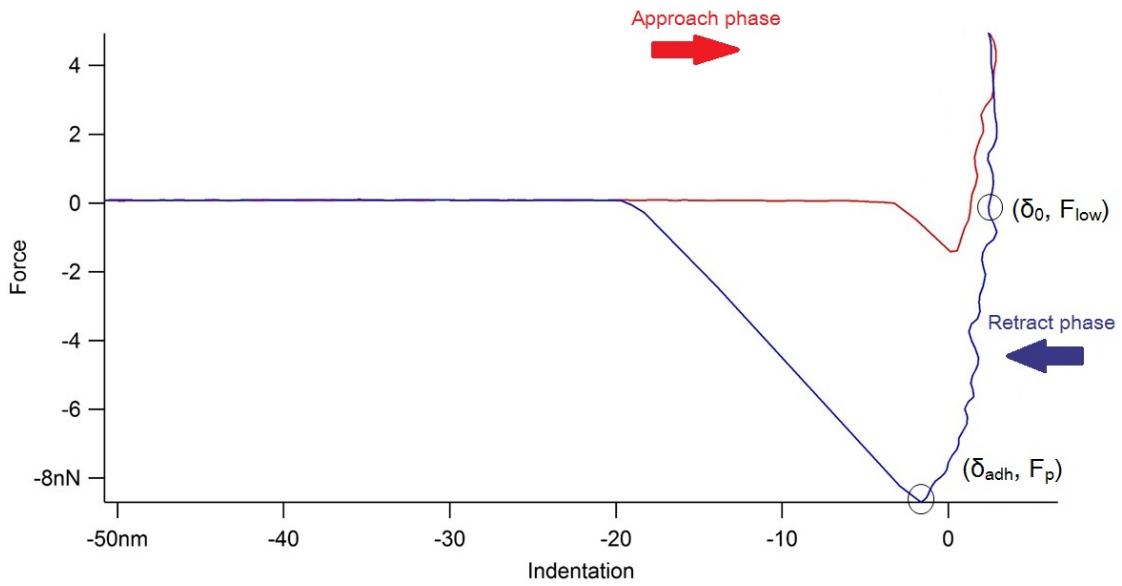

Figure 1.14: An example force curve showing the points used during a 2-point JKR analysis. Image created from figure in Ref. 55

The two important points for a 2-point JKR analysis are (δ_{adh}, F_p) and (δ_0, F_{low}),

where δ_{adh} is the AFM tip displacement at the point of maximum tip-sample adhesion, F_p is the force at the maximum tip-sample adhesion point, δ_0 is the AFM tip displacement at no applied force, and F_{low} is the applied force at tip displacement δ_0, which is equal to zero [55]. Using these two points you can calculate the reduced Young's modulus as:

$$E_r = \frac{-3F_p}{\sqrt{R}}\left[\frac{3(\delta_0 - \delta_{adh})}{1 + 4^{-\frac{2}{3}}}\right]^{-\frac{3}{2}} \tag{1.18}$$

Following the relation between reduced Young's modulus and sample Young's modulus (equation 1.14), one can get a direct equation relating the sample Young's modulus to the two points of importance on a force curve:

$$E_s = \frac{-3F_p}{\sqrt{R}}(1 - \nu_s^2)\left[\frac{3(\delta_0 - \delta_{adh})}{1 + 4^{-\frac{2}{3}}}\right]^{-\frac{3}{2}} \tag{1.19}$$

where R is the indenter radius, and ν_s is the Poisson's ratio of the sample. Ebenstein noted that the Young's modulus values obtained on samples using his 2-point JKR method, in both air and water force experiments, produced values very close to those performed in a detergent environment where adhesion forces between the tip and sample had been eliminated [55] thus showing that the 2-point JKR analysis method helps eliminate potential errors due to adhesion, resulting in more accurate determination of Young's modulus.

In more recent times, Chuan Xu, formerly of the Dr. Merschrod research group at Memorial University of Newfoundland developed a method of force curve analysis under the JKR adhesion model for his doctoral thesis [56]. This method is titled "minimum indentation JKR", as the AFM tip indents the sample only to the minimum depth required to achieve nanoindentation information. Minimal indentation of samples can be quite advantageous, especially when dealing with biological samples,

as there is a minimization of both sample viscoelastic response and sample destruction [57].

The minimal indentation JKR method to determine the Young's modulus of a sample relies on two important phenomena during a force spectroscopy experiment: the jump to contact between the tip and sample, and the jump from contact (adhesion force) of the tip and sample. As both of these parameters can be extracted directly from a force curve, using this analysis method to determine the Young's modulus is fairly quick and simple. Xu proposed the following equation to describe the Young's modulus of a sample from a minimal indentation experiment [56]:

$$E_s = \frac{5}{2}|F_p|R^{-\frac{1}{2}}(1-\nu_s^2)\left(\Delta d - 2\left(\frac{AR}{24k_c}\right)^{\frac{1}{3}}\right)^{-\frac{3}{2}} \tag{1.20}$$

where F_p is the jump-from-contact (i.e., adhesion) force, R is the AFM tip radius, ν_s is the sample Poisson ratio, Δd is the jump-to-contact distance between the tip and sample, and k is the spring constant of the tip. A is defined as the Hamaker constant, which can also be estimated from a force-distance curve by the following equation [58]:

$$A = \frac{24}{27}\frac{k_c \Delta d^3}{R} \tag{1.21}$$

1.3.1.3 Minimum Indentation JKR with Capillary Forces

When performing AFM in air at ambient conditions there can be an added capillary forces acting upon the tip. These capillary forces arise from two factors, each of which contribute to considerable tip-sample adhesion which can be problematic during force measurements. At ambient conditions the air will likely have some moisture present, known as relative humidity. The humidity results in a layer of water condensing on the sample being studied. As the tip is brought into contact with the surface, it is pulled

towards the surface by a tiny liquid meniscus as seen in Figure 1.15 [38, 59]. This pull is caused by the capillary forces, and results in a stronger tip-sample adhesion as the AFM tip is constantly being pulled towards the sample, even during retraction.

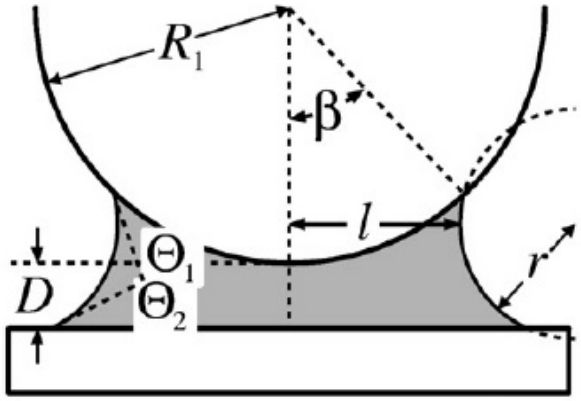

Figure 1.15: Liquid meniscus formed between a spherical indenter with radius R_1 and flat surface. D is the gap width between the indenter and surface, r and l are both the radius of curvature for the meniscus, β is the filling angle, and Θ_1 and Θ_2 are the contact angles of the liquid to the tip and surface, respectively

The degree of adhesion caused by capillary forces present has been shown to be dependent on the relative humidity of the environment. Butt and Kappl [59] performed extensive research into studying the capillary forces between a spherical object and surface, and its dependence on the relative humidity. As shown in Figure 1.16, as the relative humidity of the environment increases, as does the capillary forces between the indenter and sample, resulting in a larger adhesion force between the two. Ideally, to decrease the effect of these capillary forces, experiments would be performed under vacuum, or in a sealed environment with dry air to reduce the relative humidity. However, such setups can be costly or bulky, so alternative methods are more favored.

To account for these capillary forces when performing force curves in air, Chuan Xu also proposed a model for determining the Young's modulus from a force-distance curve which accounts for the capillary forces acting upon the tip and sample [56].

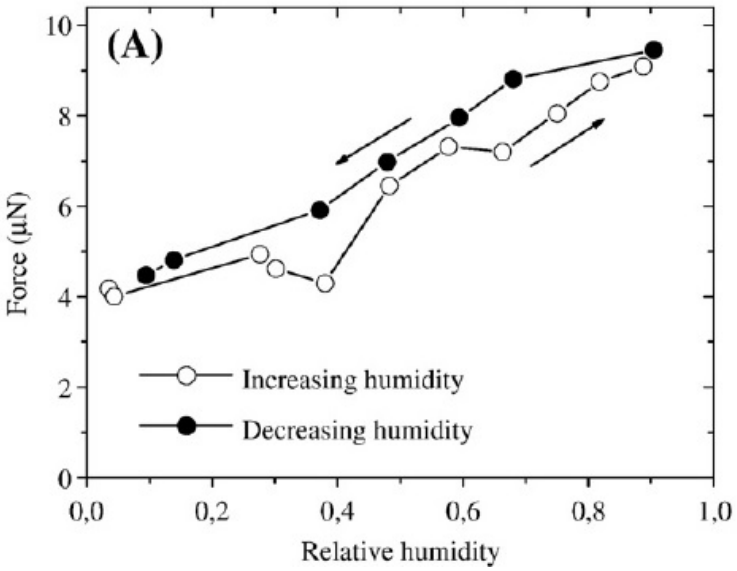

Figure 1.16: Increasing the relative humidity of the environment increases the adhesion force between the tip and sample, a result of the increase in capillary forces between the two

In his doctoral thesis, Xu broke down the total capillary force acting on the tip into two distinct parts: an attractive force acting on the tip resulting from the pressure difference across the air-water interface, and the net surface tension on the tip. Mathematically, he described the total capillary forces as:

$$F_c = \pi\gamma R\left(1 - \left(\frac{R-\delta}{R - 2\frac{\lambda_k}{\ln H}}\right)^2\right)\left(2 - R\frac{\ln H}{\lambda_k}\right) \tag{1.22}$$

where γ is surface tension of water, R is the AFM tip radius, δ is the tip indentation depth into the sample, λ_k is the Kelvin length of water (0.523 nm at 25 °C), and H is the relative humidity of the room.

Xu proposed an equation similar to the minimal indentation JKR Young's modulus (equation 1.20 in Section 1.3.1.2) which accounts for the capillary forces acting upon the tip [56]:

$$E_s = \frac{\pi\gamma\left(\frac{R}{2}\right)^{\frac{1}{2}}}{32}(1-\nu_s^2)\left(1-\left(\frac{R-\Delta d+S_o}{R-2\frac{\lambda_k}{\ln H}}\right)^2\right)^2\left(2-R\frac{\ln H}{\lambda_k}\right)^2\frac{1}{(\Delta d-S_o)^{\frac{3}{2}}} \quad (1.23)$$

where Δd is the jump to contact distance, which can be determined from the force curve, and S_o is the tip-sample separation distance. During the jump to contact phenomena, the jump to contact distance Δd can be broken down into two parts: the tip-sample separation distance, S_o, and the sample indentation distance δ. They relate to each other as follows:

$$\Delta d = \delta + S_o \quad (1.24)$$

Distinguishing the two parts of the jump to contact distance on a soft sample is extremely challenging, however the tip-sample separation distance is needed to solve equation 1.23. To do this, a force-distance curve can be performed on a hard surface such as a Si wafer, freshly cleaved Highly Ordered Pyrolytic Graphite (HOPG), or freshly cleaved mica. The indentation depth of the tip into these hard surfaces is negligible, making the jump to contact distance in this situation the same as the tip-sample separation [56]. Assuming that the humidity of the environment does not dramatically change between force curve experiments, this tip-sample separation distance will be true for all samples and can be used to solve equation 1.23.

Using this model, as well as the model seen in equation 1.20, we are able to determine the Young's modulus of samples via force spectroscopy in ambient conditions. Adhesive effects including those from tensile attractions, as well as those caused by capillary forces between the tip and sample are accounted for in these models, which give them a great advantage over using the standard Hertz model of analysis.

1.4 Thesis Summary

In this thesis, we look to examine in detail the rainbow smelt eyes tissue discussed in Section 1.1.2 using AFM. Specifically, in Chapter 2 we look to characterize the morphology of both the cold and warm water smelt eyes to determine if the adaptation has any effects on the structures of the eyes. As well, analysis of the Young's modulus of both the warm and cold water eyes will be performed to determine if there is any differences which could be attributed to the adaptation. In Chapter 3, we will analyze the effect of hydration on the morphological and mechanical properties of both subsets of Rainbow smelt eye tissue in attempt to better study the samples in an way which better represents the *in vivo* environment. Finally, results, conclusions, and future work are presented in Chapter 4. Two additional appendices are presented along with the thesis. In Appendix A, we outline the various experimental methods used in attempt to produce a working Tip-Enhanced Raman Spectroscopy (TERS) probe for analysis of the smelt eye tissues. Appendix B outlines the method for performing AFM imaging in fluid, and is meant to serve as a guided document for others within the group to follow when trying to perform in-fluid measurements using AFM.

Chapter 2

Investigating the Differences Between Cold and Warm Smelt Eye Tissue

2.1 Motivation

As concluded in Section 1.1.2, rainbow smelt have a hyperosmotic adaptation to its environment where glycerol accumulates in the vitreous humor of the eye, increasing the osmotic pressure and preventing freezing during the cold winter months [19]. Interestingly, an increase in osmotic pressure of the eye is also a consequence of diabetes in humans, as discussed in Section 1.1.1. In patients suffering from diabetic complications, the increase in osmotic pressure, among other issues [60], causes issues such as macular edema, which ultimately lead to vision loss. From this, one would expect that rainbow smelt may also suffer from similar vision problems, however this is not the case as rainbow smelt and other teleost fish rely on their vision to catch prey [61]. This raises the question as to how these fish have adapted to their hyperosmotic state

in such a way that their vision has not been impaired, and more importantly, what we can learn from this adaptation that can be applied to working towards possible treatments of human vision loss.

In this study, Atomic Force Microscopy (AFM) is used to characterize the morphological and mechanical properties of both the warm and cold water smelt eye tissue in attempt to identify any differences which may be a result of the hyperosmotic stress in the cold water smelt.

2.2 Experimental

2.2.1 Preparation of Smelt Eye Samples

Harvesting of the rainbow smelt and preparation of the eye samples was performed by Dr. Robert Gendron of the Division of Biomedical Sciences in the Faculty of Medicine at Memorial University of Newfoundland. In short, upon harvesting the fish were sacrificed by a firm blow to the head, followed by the severing of their spinal cord [19]. The eyes of the fish were removed and then frozen in optimal cutting temperature (OCT) compound. Cross sections were cut at a thickness of 7 μm using a Leica CM1900 cryostat. The cut cross sections were dried overnight at -80 °C, and then thawed and air dried for preparation on to glass slides for AFM analysis.

2.2.2 Atomic Force Microscopy

2.2.2.1 Topographic Imaging

An atomic force microscope (MFP-3D, Asylum Research) was used in contact mode to map the topography of both the cold and warm water smelt eye samples. Experiments were performed using a gold-chromium coated AFM probe (HQ:CSC37/Cr-Au,

Mikromasch) with a spring constant of approximately 0.4 N/m and resonant frequency near 30 kHz. The specific spring constant and resonant frequency for the cantilever in use during each experiment was determined using the thermal noise method [62]. Topographic images were acquired at a rate of 0.5 Hz with 256 × 256 pixel resolution, and with varied size dimensions. 90 × 90 μm scans were performed during an initial exploratory scan through the cross-section. All other AFM imaging scans ranged in size from 20 × 20 μm down to 5 × 5 μm.

2.2.2.2 Force Spectroscopy

An atomic force microscope (MFP-3D, Asylum Research) was used to perform the force spectroscopy experiments on both the cold and warm water smelt eye tissue. Experiments were performed using a gold-chromium AFM probe (HQ:CSC37/Cr-Au, Mikromasch) with a spring constant of approximately 0.4 N/m. A quick 20 × 20 μm topographic image of the area to be studied was acquired at a rate of 0.5 Hz. In some cases, subsequent 5 × 5 μm topographic scans were taken if a smaller area was desired.

The AFM tips inverse optical lever sensitivity (invOLS) was calibrated using a method outlined in the MFP-3D user manual [63]. In short, a force curve of an hard surface such as freshly cleaved mica or silicon wafer was taken. A fit to the contact region of the curve is selected, and the slope of which is the invOLS, which is required to determine the spring constant of the tip, as shown in Figure 2.1

Force curves were performed under ambient conditions, using the minimal indentation parameters outlined in Chuan Xu's doctoral thesis [56]. First, the specific spring constant and resonant frequency for the cantilever in use was determined using the thermal noise method [62]. Both cold and warm water smelt eye samples were indented by the AFM tip at a velocity of 200 nm/s and a force of 5 nN. Force map-

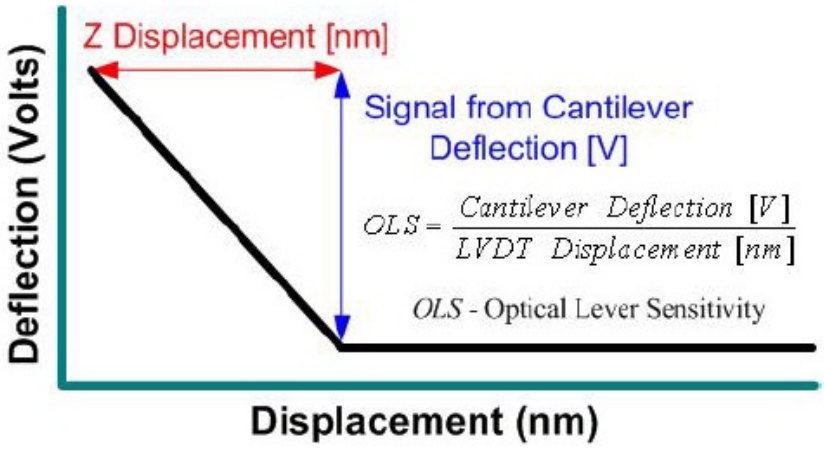

Figure 2.1: Determination of the optical lever sensitivity from a force curve of a hard surface

ping of the samples was performed at a resolution of 16 × 16 pixels, where each pixel represents a unique force curve from which the apparent Young's modulus can be determined. For all force experiments, force curves and force maps were all performed in triplicate.

2.3 Results and Discussion

2.3.1 Morphology of the Smelt Eye Tissue

To get a sense of the nanostructures of the rainbow smelt eye, an initial experiment was performed in conjunction with fellow masters student Asia Alhasawi. [64] During this experiment, AFM imaging of the cold water smelt eye cross section was performed, starting from the front of the eye and moving towards the back. This resulted in a complete set of images profiling the unique structures of the eye as the tip moved through the sample. Figure 2.2 highlights some of the different nanostructures present within the cold water smelt eye.

To help identify the areas of the eye which correlate with the topographic images

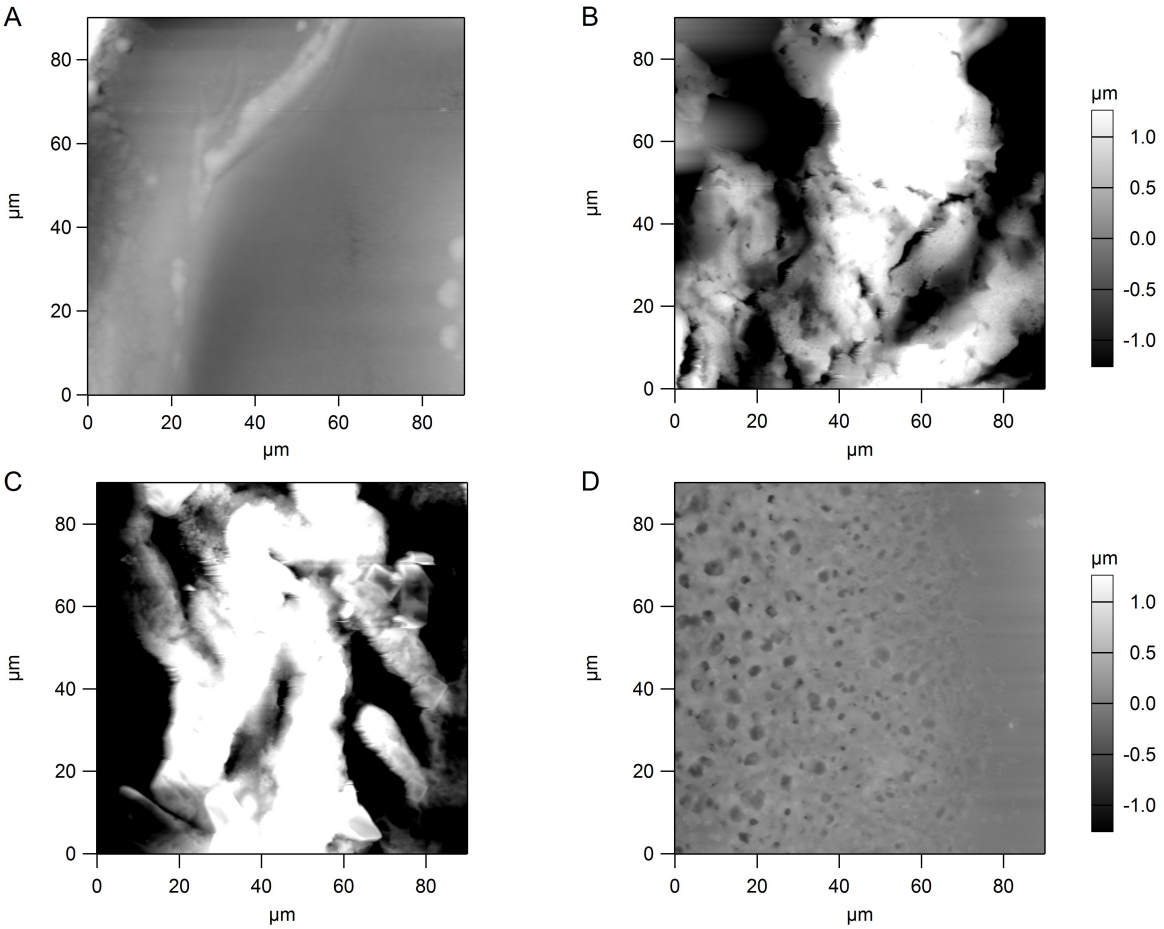

Figure 2.2: Various nanostructures found within the cold water smelt eye. A) is located near the front of the eye, B) and C) near the centre of the eye, and structure D) is located near the back of the eye

obtained, we co-ordinated with Dr. Robert Gendron. The structure shown in Figure 2.2 (D) is of particular interest, as its porous structure is particularly striking and is unique from other structures found during the exploratory scan of the eye. Given its location in the eye, along with its nanostructure, the AFM image seen in Figure 2.2 (D) is of either the retina or the choriocapillaris, which is the vascular region of the choroid. Both the retina [65] and the choriocapillaris [66] have a vast system of blood vessels which supply blood and oxygen to the eye tissue. Hence, the porous network seen in this part of the eye is a result of the blood vessels present in these eye structures.

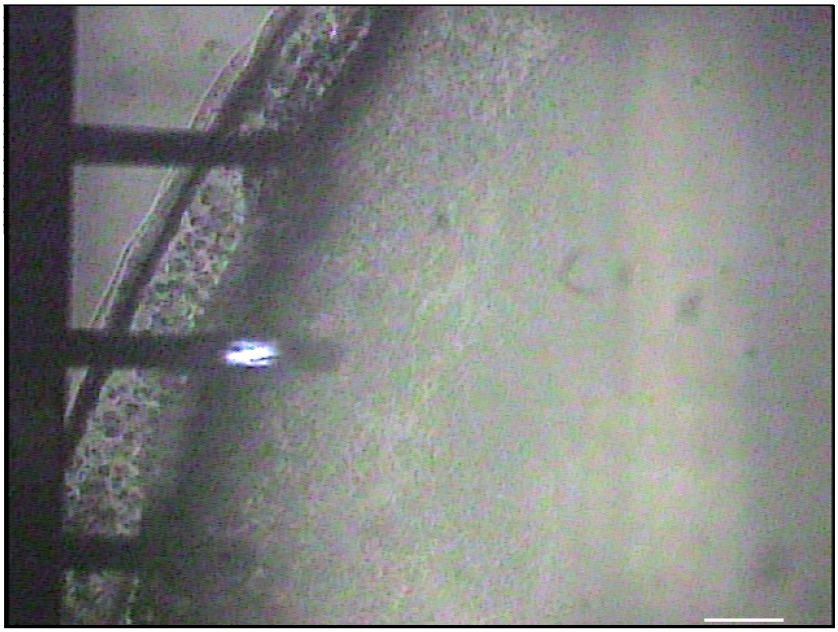

Figure 2.3: AFM camera image showing the area of the eye scanned correlating with the image shown in Figure 2.2 (D)(Scale bar = 50 μm)

A major advantage of analysing the area seen in Figure 2.2 (D) is that its nanostructure is unique and the area is very easy to identify under the AFM camera as seen in Figure 2.3. In comparison, many of the other structures within the eye aren't easily distinguishable from one another, such as Figure 2.2 (B) and (C), and are also

challenging to see under the AFM camera. As a result, the analysis of the rainbow smelt eye tissues will be focused on the area highlighted in Figure 2.2 (D) from here on in.

During analysis of the warm water smelt sample, the same vascular structure seen in the cold water smelt is present and easily identifiable under the AFM camera and topographic analysis.

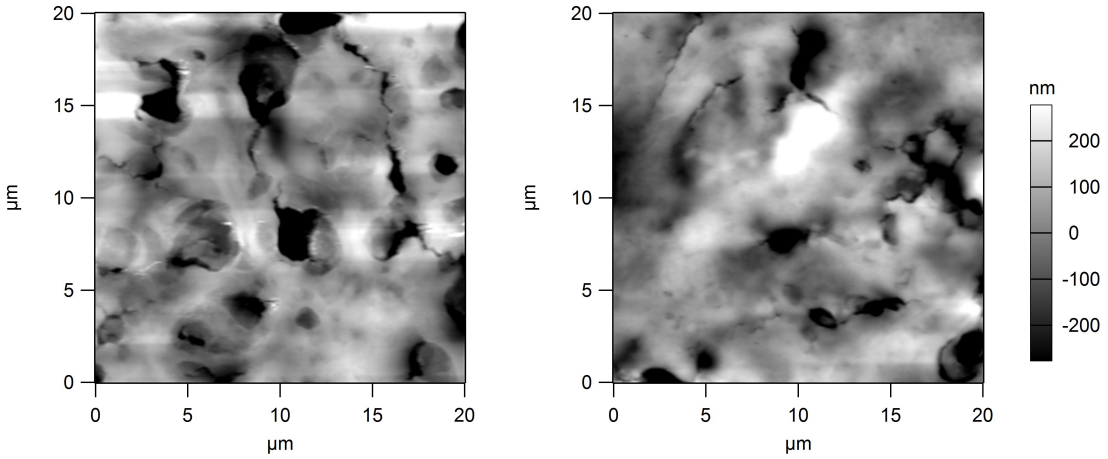

Figure 2.4: Topographic comparison of vascular region of vascular region of eye tissue between cold (left) and warm (right) water rainbow smelt

Comparison of the vascular region of both cold and warm water smelt shows two very similar AFM images (Figure 2.4). In both samples, the vascular structure of the tissue is pronounced and the only obvious feature of the scan. As seen in Figures 2.5 and 2.6, a cross section of the AFM height trace can be selected to highlight the height profile across the scan area. By doing this, analysis of the shape and depth of the vascular pore is possible.

In Figure 2.5, the analyzed pore shows a plateau at the minimum height point, indicating a flat feature at the bottom of the pore. This is a good indication that the AFM tip is indeed reaching the true bottom of the pore. From this trace, the depth of the analyzed pore of the cold water smelt was determined to be 901.0 nm.

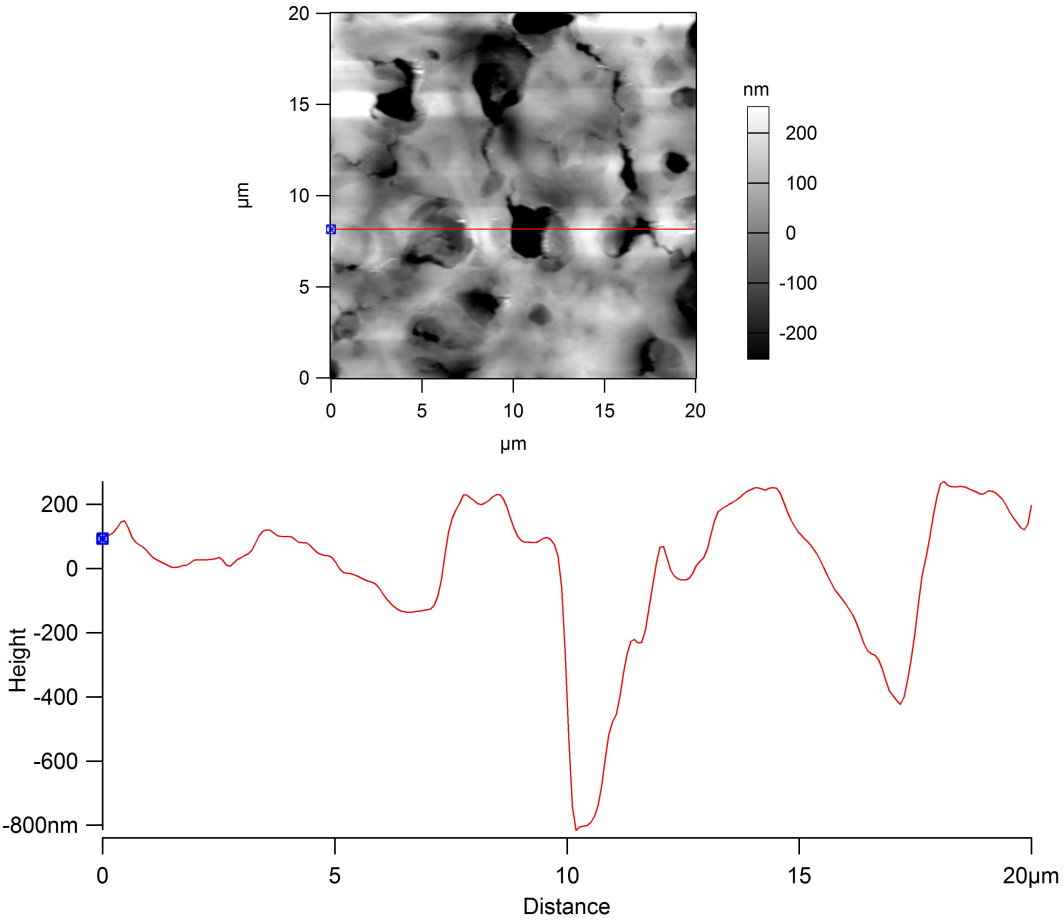

Figure 2.5: (Bottom) Height profile of the cold water smelt tissue along the red trace on the topographic image (top)

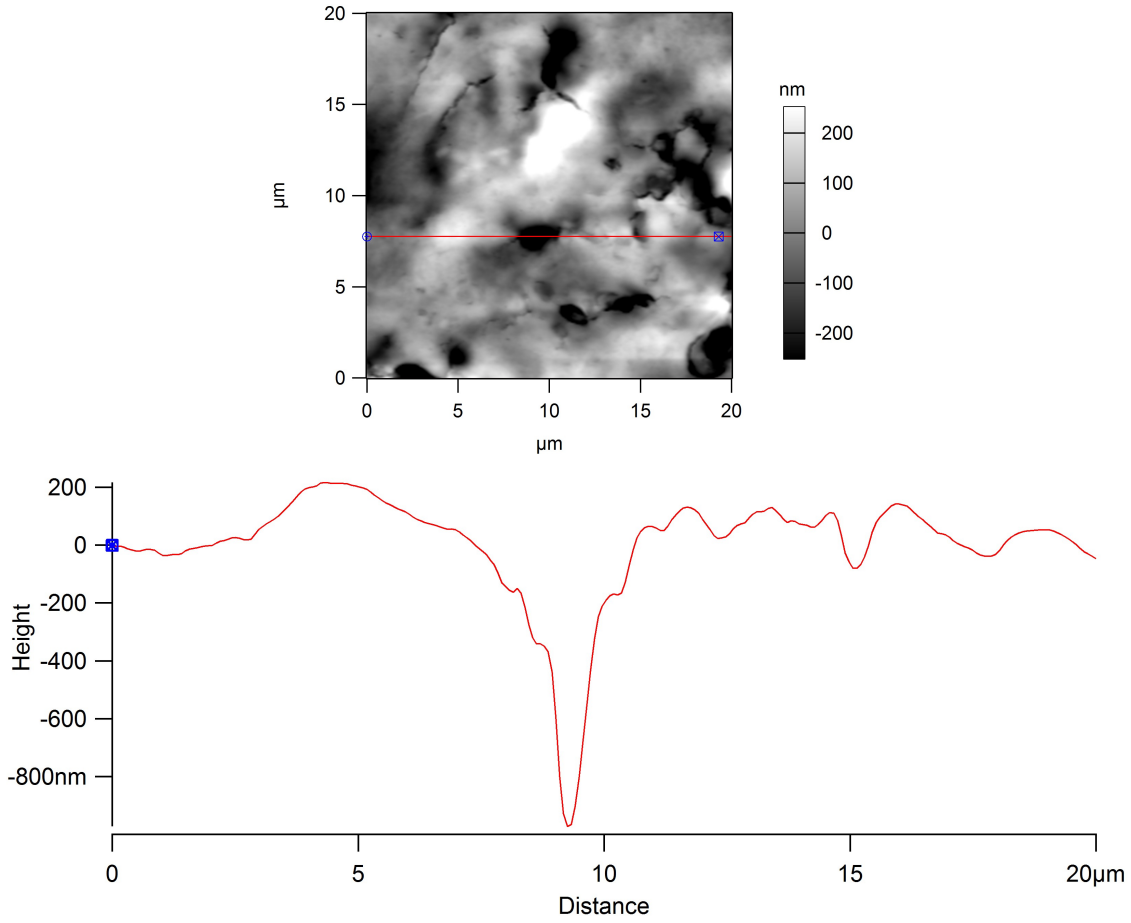

Figure 2.6: (Bottom) Height profile of the warm water smelt tissue along the red trace on the topographic image (top)

In comparison, the warm water smelt also shows a slight plateau at the bottom of the analyzed pore as seen in Figure 2.6, though this plateau is much smaller than the one seen in the cold water smelt. This once again is a good indication that our AFM probe is truly reaching the bottom of pore. From analysis of the height profile plot, the depth of the pore analyzed in warm water fish was 809.1 nm.

To assess the average pore depth of the samples in more detail, the 3D AFM topography maps of the scans seen in Figure 2.4 were analyzed to compare the average pore depth of both the warm and cold eye tissue, as seen in Figure 2.7. Visual analysis of both 3D maps show very similar pore depths between both the warm and cold water smelt eye tissues, which indicates that the hyperosmotic state seen in the cold water smelt does not induce structural change at these length scales.

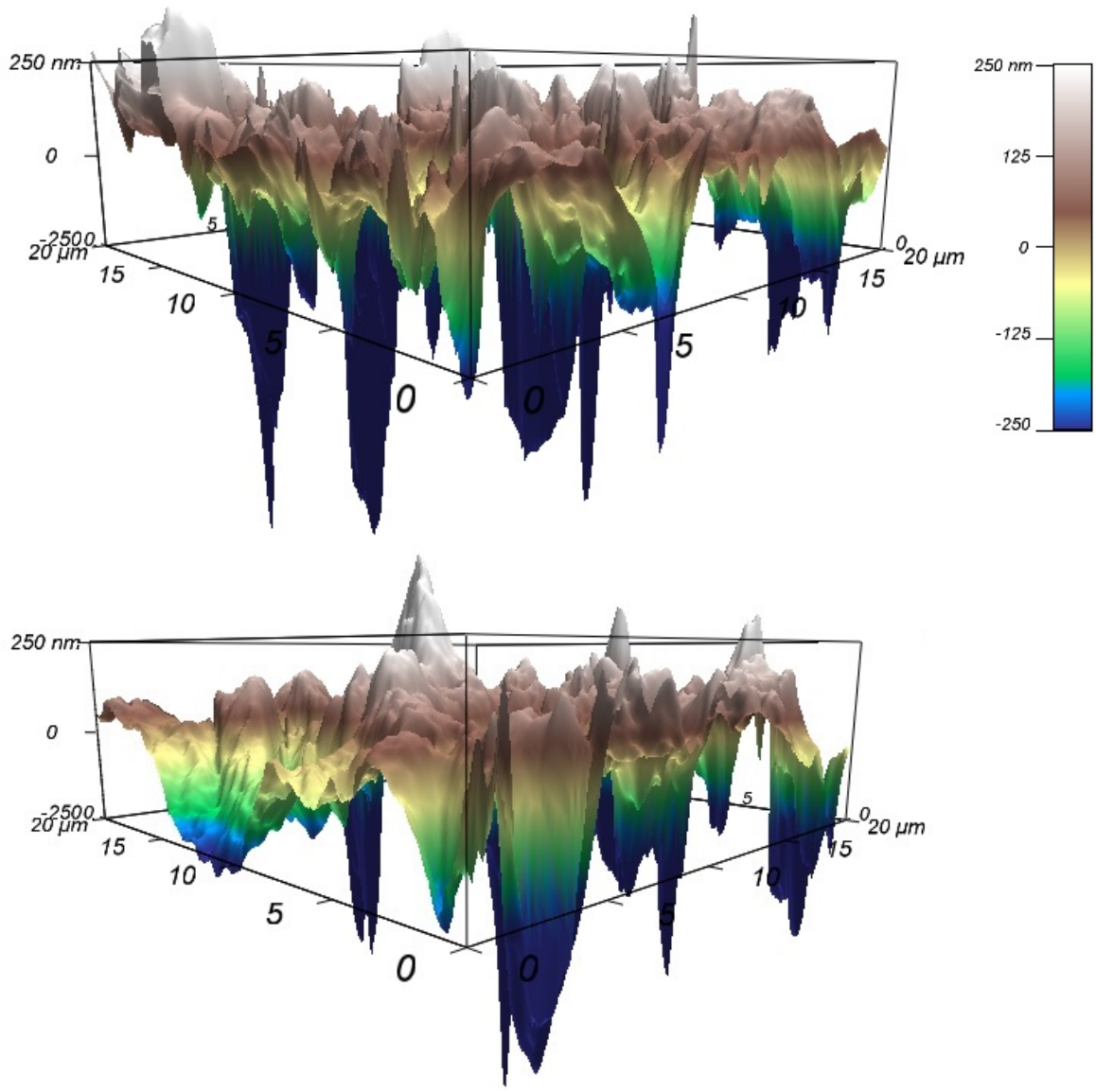

Figure 2.7: 3D topography maps of the cold water (top) and warm water (bottom) smelt eye. The Z-axis scale is the same for both maps

2.3.2 Young's Modulus of Smelt Eye Tissue

To get a sense of the mechanical properties of the whole area scanned, force mapping was performed instead of taking selected individual force curves. In force mapping experiments, a series of force curves are taken in a grid like pattern in the same manner

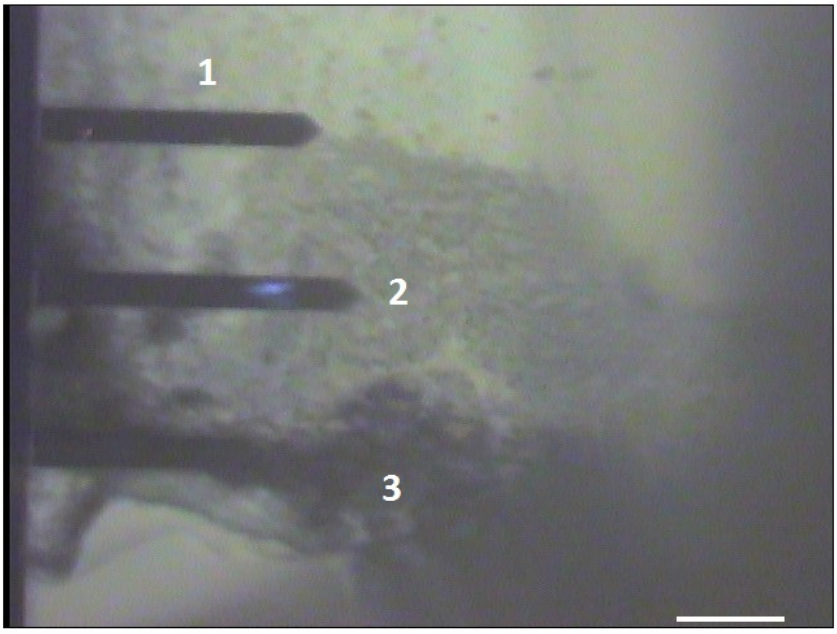

Figure 2.8: AFM camera image showing the areas where force mapping was performed on the cold water smelt sample. 1 is the area in front of the vascular tissue, 2 is the vascular tissue, and 3 is a membrane behind the vascular area of the eye (Scale bar = 40 μm)

as a typical AFM raster scan. Each force curve's data is then analyzed to extract e.g. a Young's modulus, resulting in a 2-dimensional array of force data.

To compare the cold and warm water smelt eye tissue, force mapping was performed on three areas of the samples near the vascular region identified in Section 2.2.2.1. These areas were identified by the AFM camera as follows: in front of the vascular region (area 1), within the identified vascular region (area 2), and behind this region in what appears to be a membrane (area 3). 5×5 μm AFM scans were performed first to identify the topography of the area before force mapping experiments on the area was performed.

The area of the cold water smelt eye in front of the vascular region, labelled area 1 in Figure 2.8 was analyzed first. To determine the Young's modulus, the minimal

indentation JKR model was used (equation 1.20). The average Young's modulus of the sample was determined by averaging the Young's modulus value of each point in the force map. The same procedure was completed for areas 2 and 3.

The average Young's modulus values for each area of the cold water smelt eye analysed is presented in Table 2.1. Students t-tests showed that all three values are statistically different from one another, indicating that all three areas near the vascular part of the eye have differing Young's modulus values.

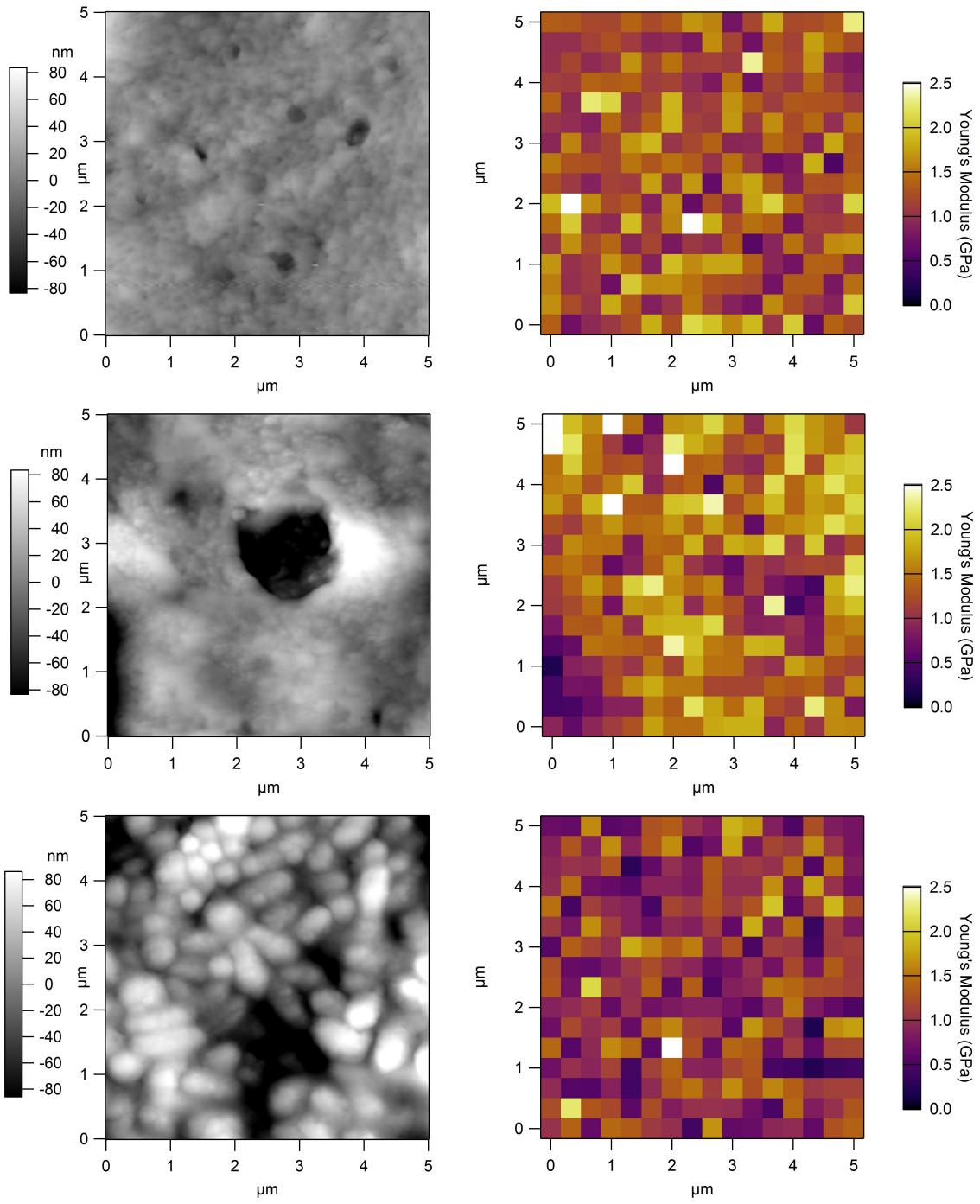

Figure 2.9: AFM height traces of the cold water smelt eye tissue before the vascular region(top left), the vascular region (centre left) and the membrane behind the vascular tissue (bottom left) with their corresponding force maps (right)

Table 2.1: Average Young's modulus values of each area analyzed under force spectroscopy for the cold water smelt tissue

	Young's modulus (GPa)	Standard Deviation (GPa)
Before vascular region (area 1)	1.291	0.37
Vascular region (area 2)	1.427	0.47
Behind vascular region (area 3)	1.042	0.39

The experiment was repeated for the warm water smelt eye tissue. Force mapping of the sample was performed in front of the vascular area, at the vascular area, and at the membrane behind the vascular region. The Young's modulus values for the warm water smelt are shown in Table 2.2 below. Students t-tests showed the Young's modulus of the vascular region is statistically different than the areas surrounding it, however there is no statistical difference in Young's modulus values between the areas before and behind the vascular region.

Table 2.2: Average Young's modulus values of each area analyzed under force spectroscopy for the warm water smelt eye tissue

	Young's modulus (GPa)	Standard Deviation (GPa)
Before vascular region (area 1)	0.803	0.24
Vascular region (area 2)	0.988	0.20
Behind vascular region (area 3)	0.809	0.34

As seen by comparing Tables 2.1 and 2.2, the average Young's modulus for the warm water smelt was lower than that for the cold water smelt in each of the three areas of the eye studied. Student's t-tests once again showed a statistical difference between the compared cold and warm tissue, confirming that the cold water smelt eye tissue analyzed is stiffer than the warm tissue.

The above data was also analyzed using the minimal indentation model which includes the capillary forces between the tip and sample (Equation 1.23), in attempt to get a more accurate Young's modulus for the samples. The same force maps seen

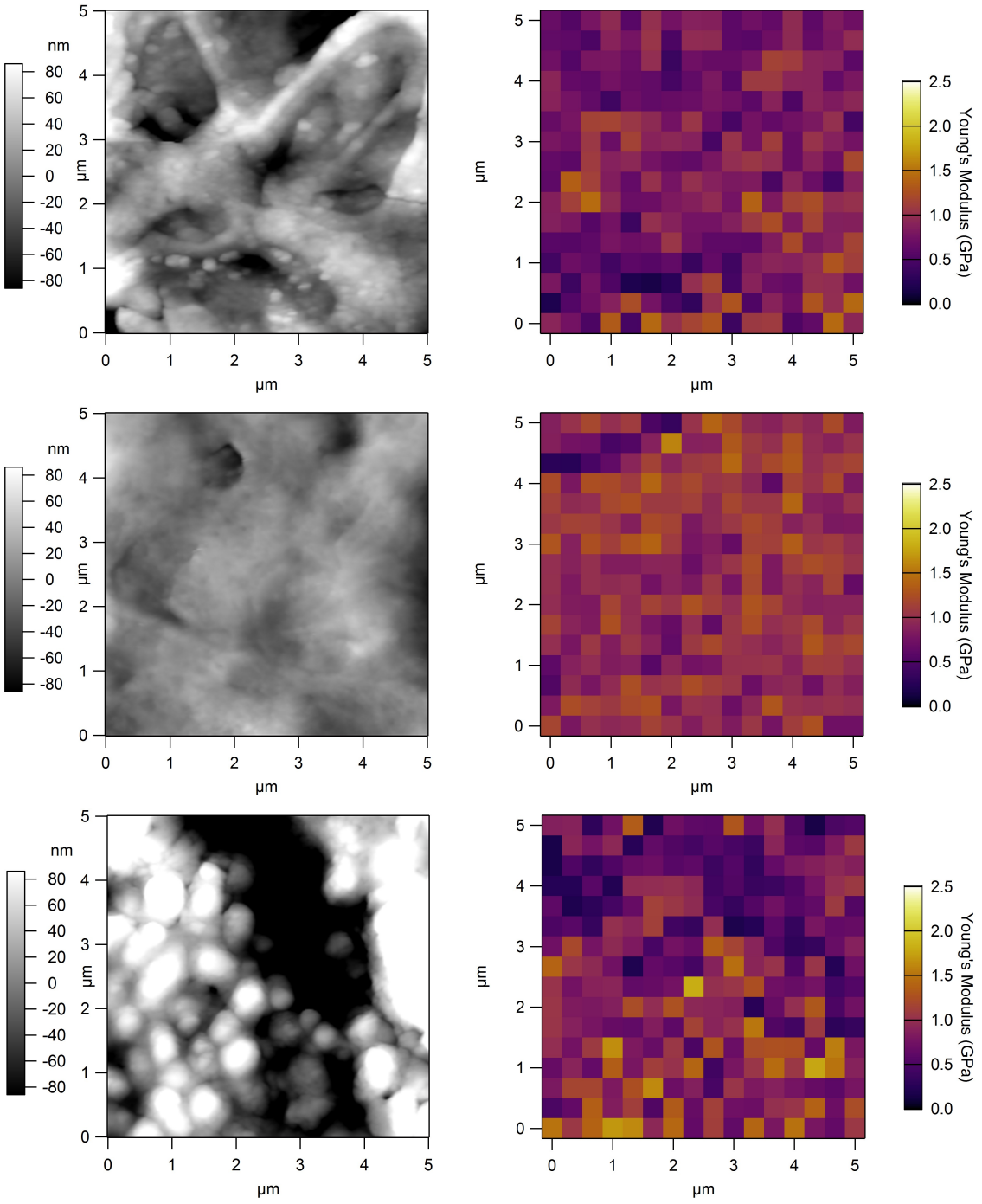

Figure 2.10: AFM height traces of the warm water smelt eye tissue before the vascular region (top left), the vascular region (centre left) and the membrane behind the vascular tissue (bottom left) with their corresponding force maps (right)

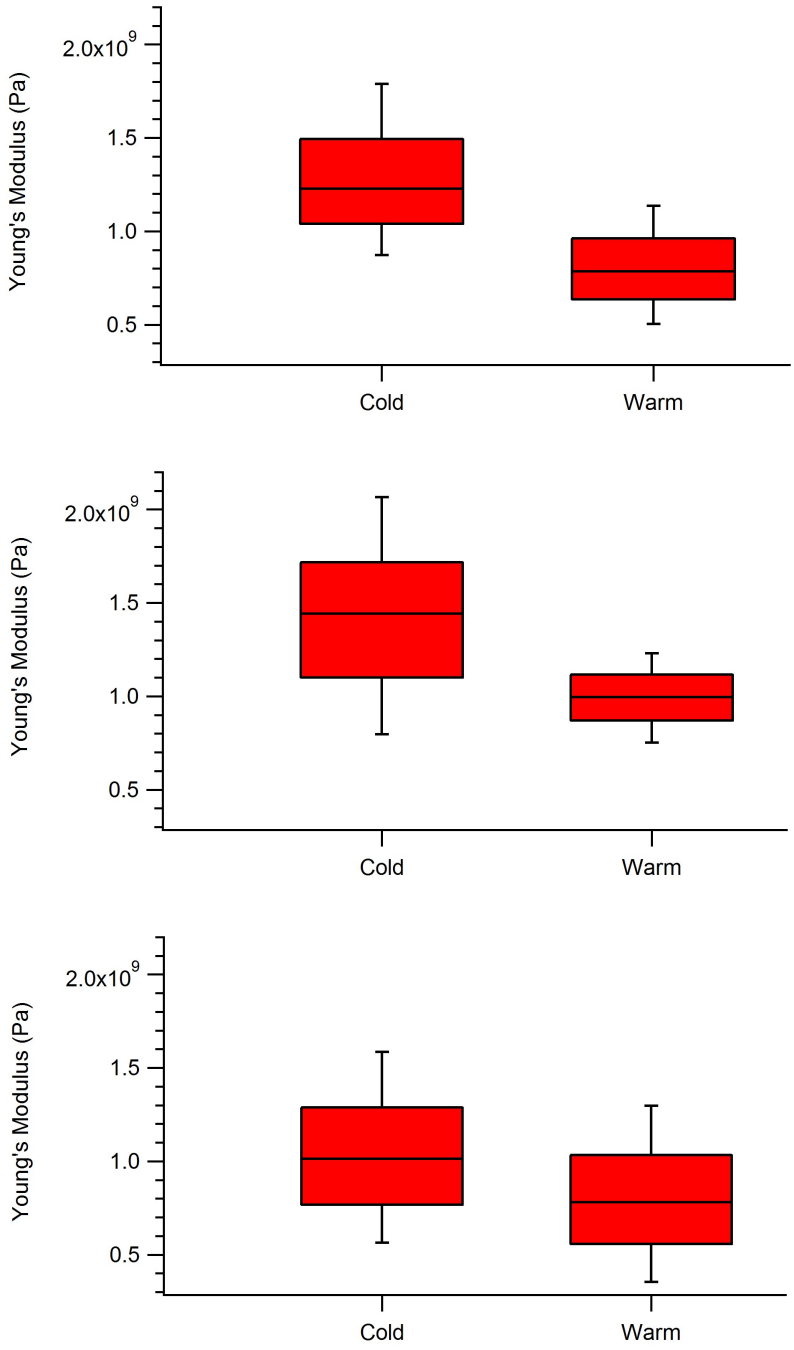

Figure 2.11: Comparison between the Young's modulus of cold and warm water smelt eye tissue before the vascular tissue (top), the vascular tissue (middle), and at the membrane behind the vascular tissue (bottom). Data for each box plot is taken from Tables 2.1 and 2.2. Each end of the box represents the upper and lower quartiles (25%) of the data, the horizontal line in the box indicates the median of the dataset, and the whiskers extend from the box to the highest and lowest value in the dataset

in Figures 2.9 and 2.10 were used in the analysis. The resulting force maps are shown in Figure 2.12, with results in Table 2.3.

Table 2.3: The average Young's modulus of the cold and warm water smelt eye tissues using the minimal indentation JKR model which includes the tip-sample capillary forces. N=6 fish (3 cold, 3 warm) with each force map performed in triplicate.

	Area of Eye	Average Young's Modulus (MPa)	Standard Deviation (MPa)
Cold Water Eye	Before vascular region	775.24	24.4
	Vascular region	822.66	59.7
	Behind vascular region	894.40	180.0
Warm Water Eye	Before vascular region	619.27	83.7
	Vascular region	420.03	165.0
	Behind vascular region	1241.22	4305.6

Analysis of the force maps once again highlights the difference in Young's modulus between the cold and warm water smelt eyes. However, upon analysis of the force maps, some significant issues were found. These issues are highlighted in the analysis in the force map of the warm water smelt eye, directly behind the vascular area near the back of the eye. During the analysis of the force curves, the automated IGOR procedure used to perform the calculation produced a number of error warnings. These warnings correlated with force curves which either were unable to have a Young's modulus value calculated, or where the calculated Young's modulus was significantly higher than expected (> 10 GPa). As mentioned above, this issue is most significantly seen in the warm water eye force maps performed behind the vascular region, resulting in a large average Young's modulus value for the sample, as well as a huge standard deviation value, making analysis and comparison between this data set near impossible. These same types of errors show up in the other force maps as well, however to a much lesser degree.

Analysis of the problem curves in the force maps was done to get a better idea of what is causing these errors. In all curves showing errors, the jump to contact distance

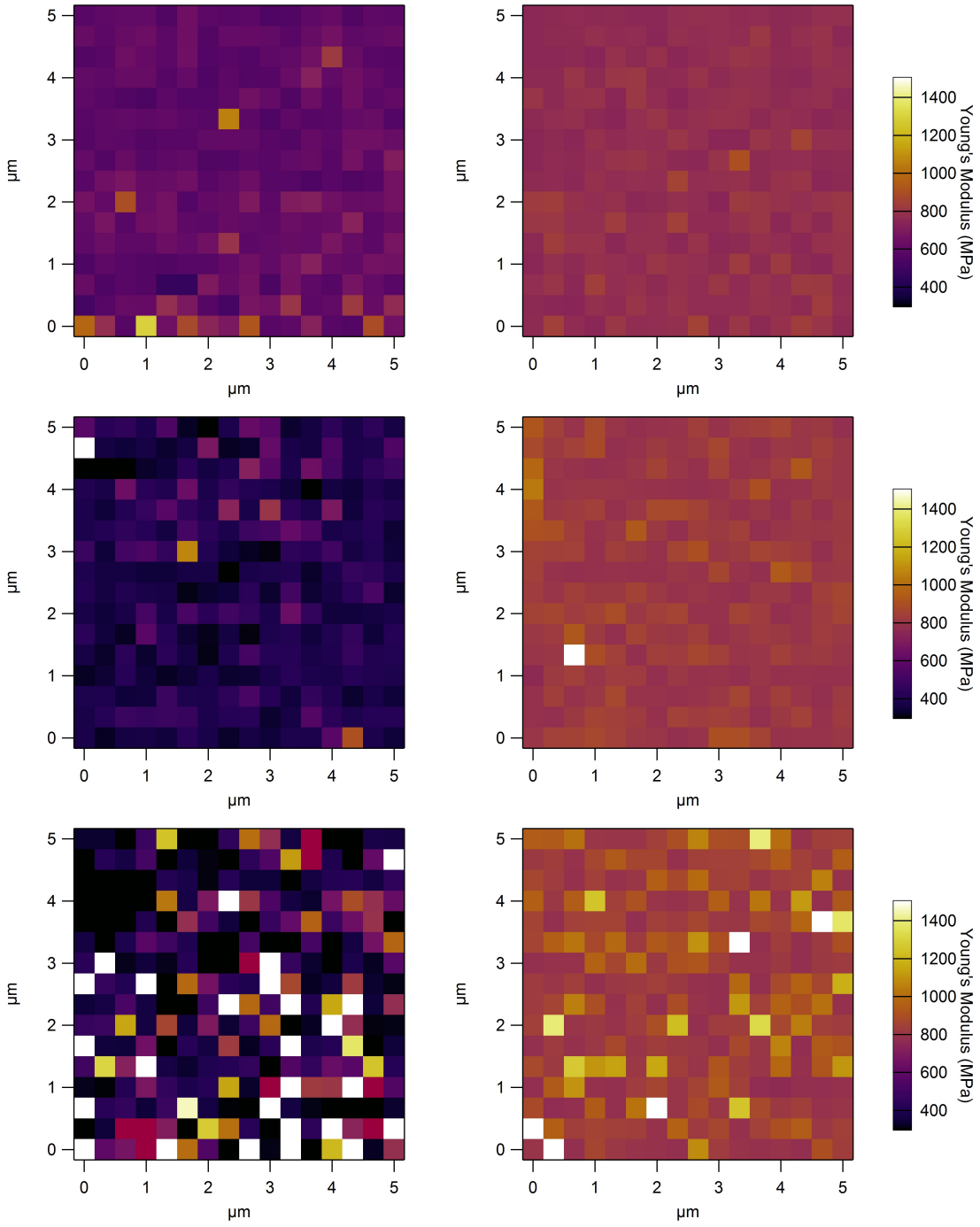

Figure 2.12: Force maps of the warm eye (left) and cold eye (right) analyzed using the capillary forces minimal indentation model. The top row shows the force maps for the analyzed areas before the vascular tissue, the middle row showing the vascular tissue, and the bottom row showing the force maps for the areas behind the vascular area

(Δd) was smaller than the estimated tip-sample distance (S_o) acquired during the tip calibration process. As dictated by Equation 1.24 outlined in Section 1.3.1.3, the jump to contact of a force curve can be broken down into two distinct parts: the tip-sample separation, along with the indentation depth into the sample (δ). If the tip-sample separation value determined during calibration is larger than the jump to contact distances seen during the force mapping experiment, then Equation 1.24 can't be satisfied unless the indentation depth of the sample is negative. As this is not possible, there appears to be an issue with the initial calibration of the tip which determines the tip-sample separation.

One explanation could be that the tip-sample separation was determined during the calibration for the relative humidity in the room during the beginning of the experiment. As stated in Section 1.3.1.3, the tip-sample separation when taking a force curve is the same for any sample given the ambient relative humidity is the same. However, our AFM is placed in a non-climate controlled room, where the relative humidity can fluctuate throughout the day. This was especially true during the force mapping experiment on the warm water smelt eye sample, where the relative humidity of the room during calibration of the tip was 50 %, but had risen to 66 % for the force mapping experiment of the area of the eye behind the vascular region. This difference in ambient relative humidity could have an effect on the tip-sample separation distance, which is not being accounted for by the calibration.

It should be noted that with the cold water smelt eye force mapping experiment, the ambient relative humidity held steady at 43-44 % throughout the entire duration of the experiment. Nonetheless there were still some force curves with jump to contact distances less than the calibrated tip-sample distance, albeit to a much lesser degree than in the warm water eye experiment. This indicates that there may be other problems within this method of data collection and analysis which were not

previously reported. While under ideal conditions, analyzing our data using the minimal indentation model which accounts for the capillary forces would give a more accurate picture of the samples Young's modulus, more work on the model is required to understand why exactly the tip-sample distance calibration isn't as accurate as desired. For this reason, further comparison of the average Young's modulus of the dried smelt eyes will be done using the standard minimal indentation JKR model.

As can be seen from the results in Tables 2.1 and 2.2, as well as the plots in Figure 2.11, the average Young's modulus of the vascular region of the eye is higher in cold water smelt than the warm water smelt. While the reason behind the stiffening of the eye tissue is currently unknown, we propose two possible theories behind this phenomena.

First, as discussed in Section 1.1.2, the cold water smelt are able to withstand colder ocean temperatures by increasing the osmotic pressure of their bodily fluids, including in the vitreous humor of the eye. This increase in osmotic pressure is directly related to the increase in glycerol and other osmolyte concentrations in the fluids. While glycerol is the major compound present which can be attributed to the increased osmotic pressure within the bodily fluids, studies have shown that increasing glycerol concentrations in protein films has a plasticizing effect, resulting in a decrease in the films Young's Modulus [67,68]. Urea, another osmolyte found in the cold water smelt, has been found to increase the Young's modulus of materials when present, which could account for the apparent stiffening in the cold water smelt eye tissue [69]. Also present in the cold water smelt are anti-freeze proteins, which are known to also aid in the prevention of freezing in cold water environments [70]. While no current work has been performed correlating antifreeze proteins to mechanical properties in teleost fish, other studies have been performed on the presence of similar antifreeze proteins present in the tissues of carrots [71]. In that study, the presence of antifreeze protein

was found to both increase the tissue rigidity as well as the Young's modulus, resulting in stiffer tissue. Ultimately, more work will have to be completed to determine if either of these factors can be attributed to the increase in Young's modulus of the cold water smelt eye tissue, which will be further discussed in Chapter 4.

Another possible explanation for the increased Young's modulus in the cold water smelt eye was outlined in a paper published by E. Crockett [72]. In that paper, the lipid membranes of several ectotherms were studied at both warm and cold temperatures. It was discovered that significant lipid membrane restructuring occurs within these ectotherms at lower environmental temperatures. The most common membrane restructuring phenonema seen involves an increase in the degree of unsaturated fatty acids within the membranes at colder temperatures. Further studies have shown that lipid membranes with higher degrees of polyunsaturated fatty acids are more susceptible to lipid peroxidation [73].

As lipid peroxidation rates are higher at warmer temperatures, it would be expected that the rates of lipid peroxidation for membranes in colder environments would be much slower. However, some degree of lipid peroxidation is required to produce byproducts which aid in cellular processes [74]. Hence, it is hypothesized that lipid membrane restructuring to increase the degree of polyunsaturated fatty acid chains is an attempt to allow easier lipid peroxidation at the colder temperatures. The difference in average Young's modulus values between the warm water and cold water smelt fish eye samples could be attributed to the difference in polyunsaturated fatty acid compositions of the lipid membranes in the two eyes, caused by the lipid restructuring.

2.4 Conclusions

Analysis of the rainbow smelt eye samples identified several distinct and unique microstructures present within the eye using AFM. This is the first time that such a collection of AFM images corresponding to different microstructures of the eye has been performed. We were able to identify the vascular micostructure located near the back of the eye as either the choriocapillaris or retina, both of which are blood-vessel dense areas near the back of the eye which supply the eye with blood, oxygen, and other nutrients. This work will enable future studies to definitively correlate AFM topography with structures traditionally identified through other types of microscopy.

Comparison of the topographical and mechanical properties of the vascular region of the eye for the cold and warm water smelt eye samples was performed. Comparison of the structure of the vascular region between the cold and warm smelt eye showed no real difference between the two, with both the vascular topography as well as the vascular pore depth being the same between the two eyes. However, we determined that the average Young's modulus of the cold water smelt eye was larger than that of the warm water smelt. As the changing stiffness did not arise from microscale changes in structure, this indicates that a molecular-scale change which occurs during the acclimatization to the cold water environment is causing the tissue in this region of the eye to become stiffer.

Chapter 3

The Effect of Hydration on Smelt Eye Tissue

3.1 Motivation

When studying biological materials with Atomic Force Microscopy (AFM), consideration of whether or not analysis of dried samples will give accurate results is required. Many of the force spectroscopy studies on biological samples in the literature are performed on hydrated rather than dry samples [49, 75, 76]. This desire to perform AFM experiments in fluid is in attempt to better model the experimental conditions after what one would expect *in vivo*. Analysis of biological samples such as cells, tissues, or proteins, in a fluid environment will better represent the samples true properties over dried samples analyzed under ambient conditions.

Previous work done by Grant *et. al* on the differences of collagen fibrils properties in air and fluid best represents the need to focus on in-fluid analysis. In their study, they found that hydrating collagen fibrils resulted in a swelling of the proteins, increasing their overall diameter as well as a decrease in Young's Modulus of 2-3 or-

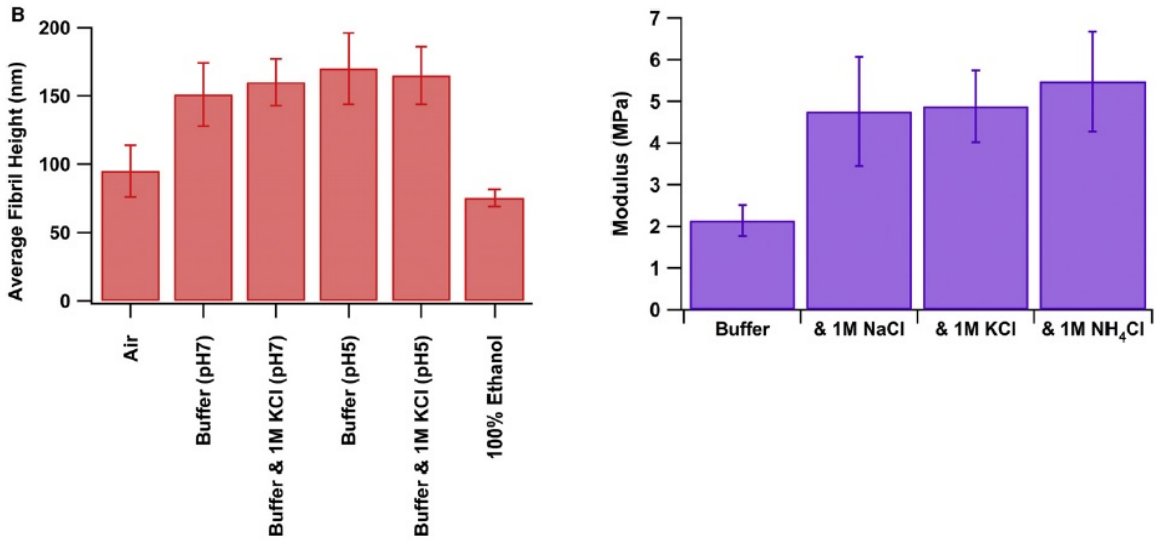

Figure 3.1: Effects of hydrating collagen fibrils with various buffer and salt solutions on its average fibril height (left) and Young's modulus (right) [77]

ders of magnitude as outlined in Figure 3.1 [77]. Furthermore, they noticed that the Young's modulus of the collagen fibrils was dependent on the types of ionic species present in the hydrating solution, and that there appeared to be a correlation between increased ionic strength and increased Young's modulus.

Up until now, the analysis of the smelt eye tissue has been completed under ambient conditions only. While this serves as a good starting point for comparison of the topographic and mechanical properties between the cold and warm water smelt, analysis of the hydrated samples will give a more accurate depiction of these properties. In this experiment, we aim to highlight the differences between the dried and hydrated smelt eye samples, as well as compare the Young's modulus values between the hydrated cold and warm water smelt eye tissue. As well, the effect of the ionic strength of the hydrating solution used during scanning on the Young's modulus of the sample is investigated.

3.2 Experimental

3.2.1 Topographic Imaging in Air

An atomic force microscope (MFP-3D, Asylum Research) was used in contact mode to map the topography of both the cold and warm water Smelt eye samples. Experiments were performed using a gold-chromium coated AFM probe (HQ:CSC37/Cr-Au, Mikromasch) with a spring constant of approximately 0.4 N/m and resonant frequency near 30 kHz. The specific spring constant and resonant frequency for the cantilever in use during each experiment was determined using the thermal noise method [62]. Topographic images were acquired at a rate of 0.5 Hz with 256 $\times$ 256 pixel resolution, and with varied size dimensions. Scan size varied, ranging from 20 $\times$ 20 μm down to 5 $\times$ 5 μm.

3.2.2 Topographic Imaging in Water

To image in water, an initial topographic scan was performed in air as outlined in Section 3.2.1 to determine the desired area for in-fluid analysis. Experiments were performed using a gold-chromium coated AFM probe (HQ:CSC37/Cr-Au, Mikromasch) with a spring constant of approximately 0.4 N/m and resonant frequency near 30 kHz. Upon completing the initial in-air scan, the AFM head is raised approximately 1 μm as measured by the knob on the MFP-3D head. 50 μL of 18.2 MΩ·cm ultrapure water was collected using a micropipette (Fisherbrand) and added between the sample and AFM tip holder as seen in Figure 3.2.

The specific spring constant and resonant frequency for the cantilever in use during each experiment was determined using the thermal noise method [62]. Imaging was performed in tapping mode, with a scan rate of 0.5 Hz and a resolution of 256 $\times$ 256 points and lines. Scan sizes varied, ranging from 20 $\times$ 20 μm down to 5 $\times$ 5 μm.

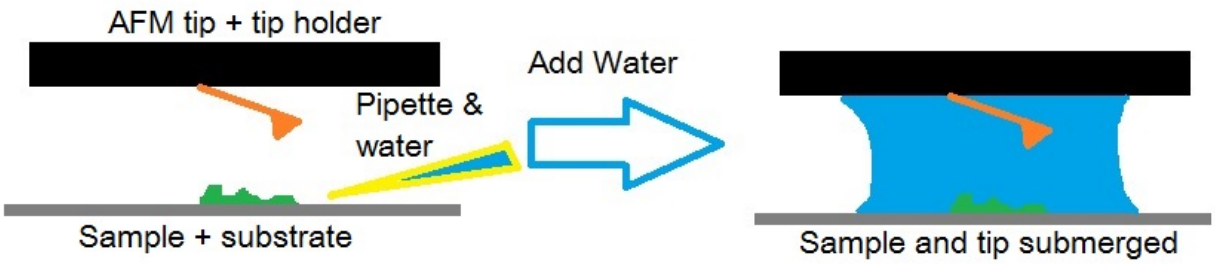

Figure 3.2: Adding water to AFM setup to allow for imaging in fluid

3.2.3 Force Mapping in Fluid

An atomic force microscope (MFP-3D, Asylum Research) was used to perform the force spectroscopy experiments on both the cold and warm water smelt eye tissue. Experiments were performed using a gold-chromium AFM probe (HQ:CSC37/Cr-Au, Mikromasch) with a spring constant of approximately 0.4 N/m. A quick topographic image of the area to be studied was acquired at a rate of 0.5 Hz. The AFM tips inverse optical lever sensitivity (invOLS) was calibrated using the method outlined in Section 2.2.2.2. This calibration was performed in water as opposed to air to better reflect the experimental conditions.

Force maps were performed in water, with a tip velocity of 200 nm/s and a trigger force of 10 nN. Both the cold and warm water smelt eyes were analyzed using the same method. Force mapping of the samples was performed at a resolution of 16 $\times$ 16 pixels, where each pixel represents a unique force curve from which the apparent Young's modulus can be determined. For all force experiments, force curves and force maps were all performed in triplicate.

3.2.4 Force Mapping and Varying Ionic Strength

An atomic force microscope (MFP-3D, Asylum Research) was used to perform the force spectroscopy experiments on both the cold and warm water smelt eye tissue.

Experiments were performed using a gold-chromium AFM probe (HQ:CSC37/Cr-Au, Mikromasch) with a spring constant of approximately 0.4 N/m. The same calibration procedure outlined in Section 3.2.3 is used in this experiment.

For both the warm and cold water smelt eye, initial 16 × 16 pixel force mapping was performed in 25 μL of ultrapure water, with a trigger force of 10 nN and a tip velocity of 200 nm/s. To increase the ionic strength of the fluid being used in the experiment, the AFM head was raised approximately 1 μm to allow enough room between the head and sample to add solution. 25 μL of 0.9985 M NaCl stock solution was added to the water droplet between the sample and AFM tip. 15 minutes was allowed for the system to equilibriate. 16 × 16 pixel force mapping was performed using the same experimental parameters noted above. This process was repeated for a total of three 25 μL NaCl additions.

3.3 Results and Discussion

3.3.1 Topographic Changes Upon Hydration

To compare the effect of hydration on the eye tissue, each eye sample was scanned dry, hydrated, allowed to equilibriate, and then scanned again. For the warm water smelt, this result is highlighted in Figure 3.3.

A dramatic difference between the dry and hydrated vascular tissue of the warm eye. The hydrated eye sample appears to swell, resulting in a much more porous and rough topography. To probe the swelling effect more, analysis of the pore depth between the dry and hydrated eye sample was performed (Table 3.1).

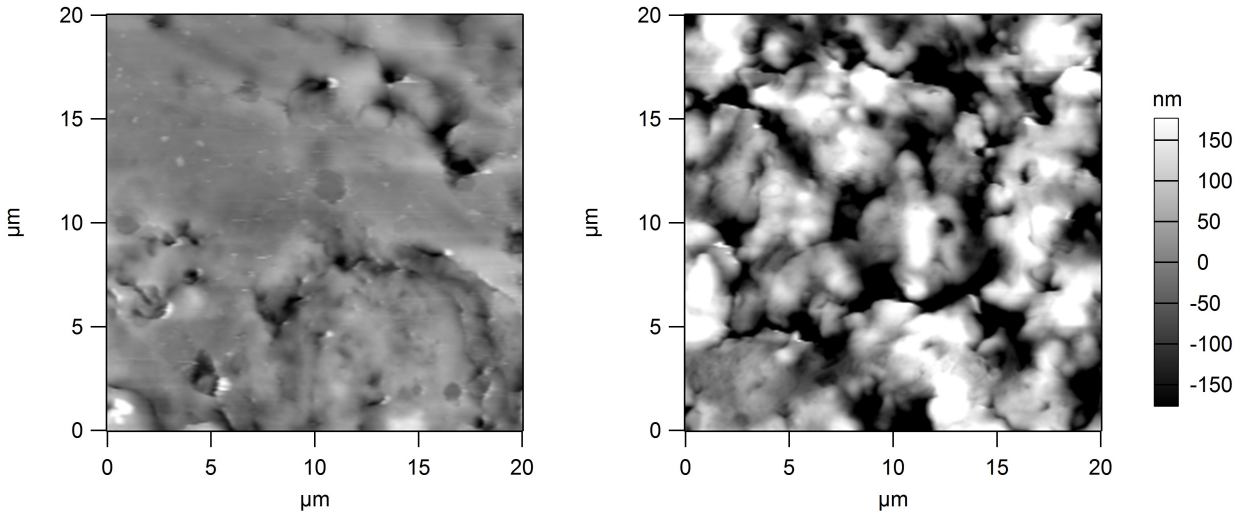

Figure 3.3: Highlighting the difference in topography between the dry (left) and hydrated (right) warm water smelt eye tissue

The effect of hydrating the tissue resulted in approximately a 3 fold increase in pore depth. Student's t-Test analysis confirmed that the difference between the dry and hydrated tissue pore depth was statistically different (P=0.002). Compared to the 2 fold swelling of the collagen fibrils upon hydration [77], this degree of tissue swelling during hydration is typical.

Table 3.1: Average pore depth of dry vs. hydrated warm water smelt eye tissue (N=3 fish)

	Average Pore Depth (nm)	Standard Deviation (nm)
Dried Tissue	206.0	62.8
Hydrated Tissue	690.3	134

The same effect can be seen in the hydrated cold water eye tissue as seen in Figure 3.4. Hydration of the tissue results in an approximate 1.5 fold increase in pore depth (Table 3.2), comparable to the before cited 2 fold swelling seen in the literature. The Student's t-Test indicates that we cannot say for certain that the pore depths between the dry and hydrated tissue are statistically different (P=0.07). Nonetheless, the effect of swelling caused by the hydration of the tissue is again visible.

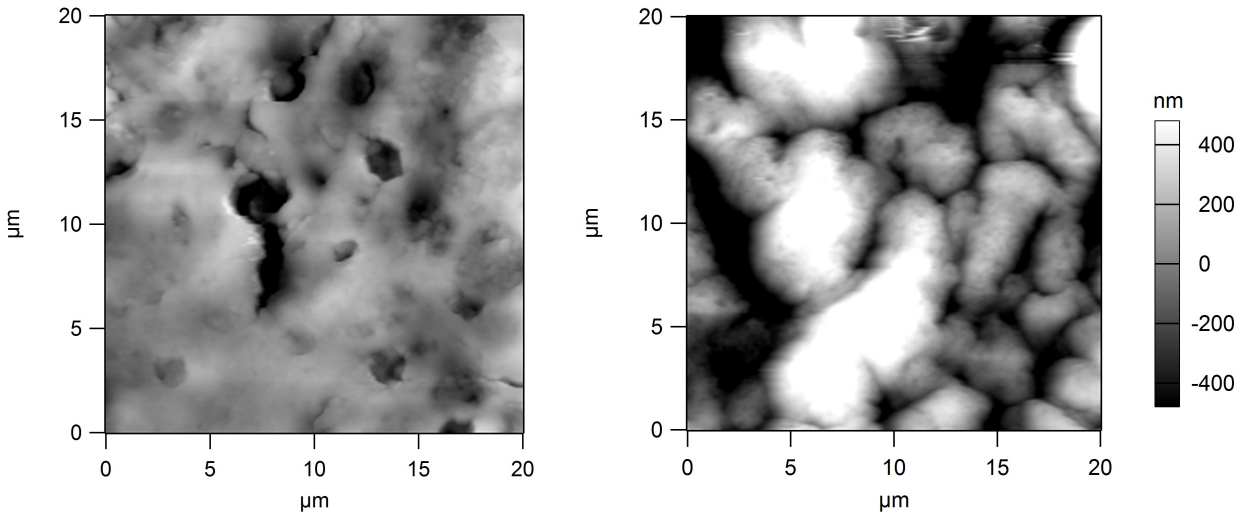

Figure 3.4: Highlighting the difference in topography between the dry (left) and hydrated (right) cold water smelt eye tissue

Table 3.2: Average pore depth of dry vs. hydrated cold water smelt eye tissue (N=3 fish)

	Average Pore Depth (nm)	Standard Deviation (nm)
Dried Tissue	728.9	281.4
Hydrated Tissue	1207.7	332.5

This method of investigating pore size is good for giving a general idea about the degree of tissue swelling that occurs during hydration. However, during hydration the tissue is also expanding in height along with the swelling of the pores. To account for this, a comparison was made between the highest and lowest height feature in

each scan, in both the dry and hydrated tissue as seen in Table 3.3. The distance between the high and low point is labelled the height difference. A swelling ratio is then defined by:

$$\text{Swelling Ratio} = \frac{\text{Height Difference (Hydrated)}}{\text{Height Difference (Dry)}} \tag{3.1}$$

Table 3.3: Height differences between the highest and lowest point in the height scan, and the swelling ratio (height difference wet/height difference dry)(N=12)

	Height Difference (nm)	Standard Deviation (nm)	Swelling Ratio
Cold Eye Dry	1629.6	185.2	**1.5**
Cold Eye Hydrated	2451.0	1095.9	
Warm Eye Dry	1109.2	540.9	**1.6**
Warm Eye Hydrated	1821.7	457.3	

From the numbers in Table 3.3, both the warm and cold eye tissue have the same approximate swelling ratio, which is very close to the two fold increase in collagen fibrils seen in the study by Grant *et. al* [77]. The larger height difference values for the cold over the warm eye tissue also reflects the larger pore size found in the analysis of the pore depths during this study.

The swelling of the eye tissue seen during our experiment can be attributed to osmotically driven hydration of the sample [77]. When ultrapure water is introduced between the sample and AFM tip, solute concentrations from within the cells are much larger than the surrounding water medium. As discussed in Chapter 1.1, this imbalance of solute concentration results in a hypotonic extracellular environment. This results in a net flow of water inward into the cell environment, causing swelling of the eye sample.

3.3.2 The Effect of Hydration on Young's Modulus

Force mapping was performed on 5×5 μm areas of the vascular region of the smelt eye tissue and the Young's Modulus values were compared between the dry and hydrated tissue. For the hydrated tissues, the Hertz model outlined in Section 1.3.1.1 was used to determine the Young's modulus. This is because when in fluid, the tip-sample adhesion force that we normally see in ambient force spectroscopy is negligible. As well, the jump to contact phenomena, a large part of Chuan Xu's minimal indentation models, [56] isn't present in fluid. As such, the Hertz model will be used to determine the Young's modulus of hydrated samples, where the minimal indentation JKR model will continue to be used for dry samples.

First, the warm water smelt eye tissue was analyzed. The dry topography scan and Young's modulus values were discussed in Section 2.3.2. The sample was then hydrated and allowed to equilibriate in the ultrapure water for 15 minutes. The height scans and corresponding force maps can be see in Figure 3.5

Analysis of the force map data provides us with the average Young's modulus of both the dry and hydrated tissue, as seen in Table 3.4. The effect of hydration has a profound effect on the average Young's modulus of the eye tissue, as the hydrated eye sample has a decrease in Young's modulus of approximately 3 orders of magnitude. This size of reduction is comparable to what has been found in the literature, where hydration of biomolecules such as collagen fibrils resulted in an approximate 2-3 orders of magnitude decrease in apparent Young's Modulus [77, 78].

Table 3.4: Comparison of the average Young's modulus values of the dry and hydrated *warm water* smelt eye tissue (N=3)

	Average Young's Modulus (MPa)	Standard Deviation (MPa)	Statistically Different? (P value)
Dry	988.2	200.9	**YES** ($P=7\times10^{-181}$)
Hydrated	1.230	0.69	

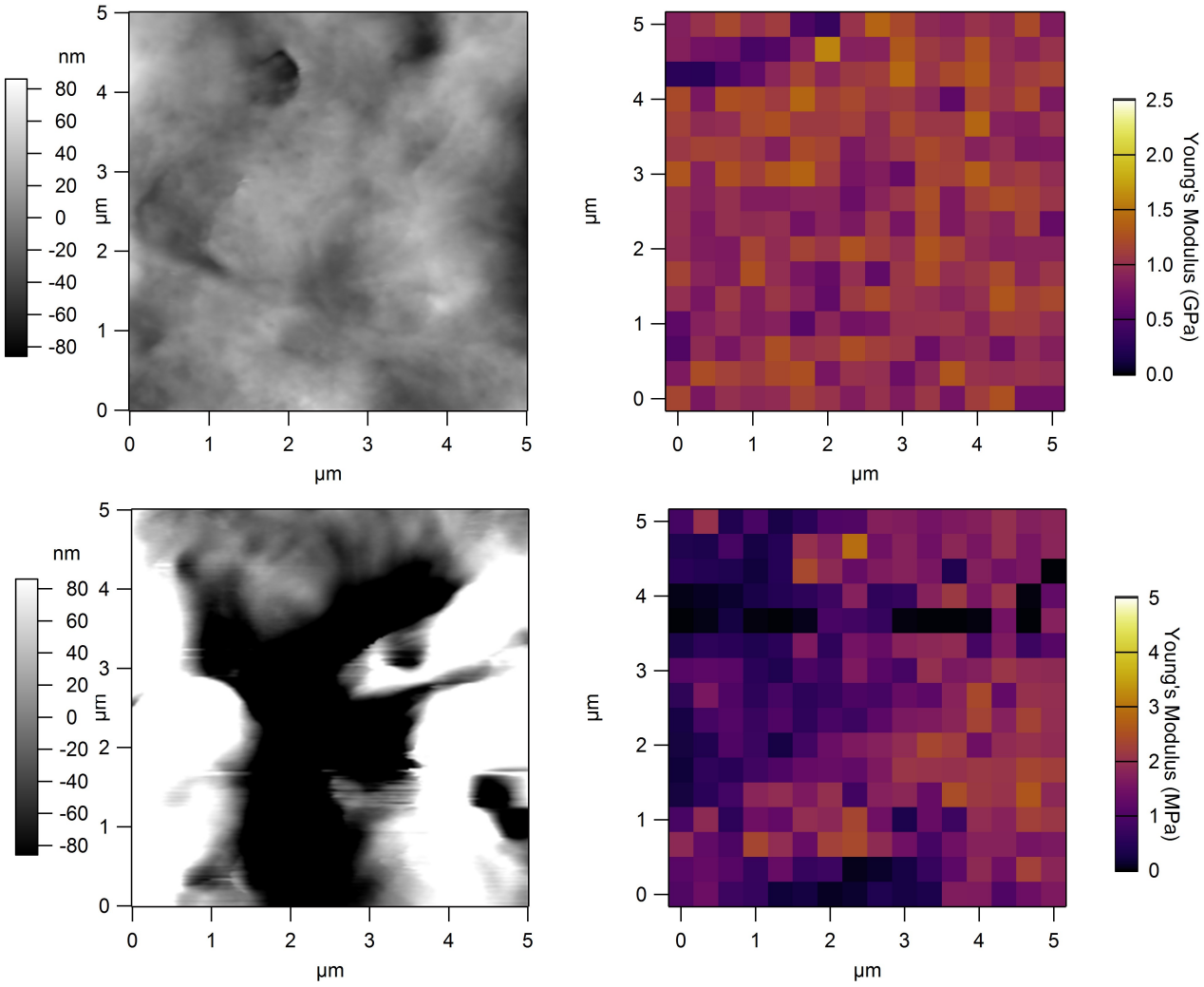

Figure 3.5: Highlighting the topography and force maps of the warm water rainbow smelt eye tissue. Top left: height image of the dry eye tissue, with its corresponding force map (top right). Bottom left: height image of the hydrated eye tissue, with its corresponding force map (bottom right)

The same method was performed on the cold water rainbow smelt eye, which can be seen in Figure 3.6. Once again, the Young's modulus of the vascular area of the eye decreased upon hydration as seen in Table 3.5. In similar fashion to the warm water sample, the average Young's modulus of the cold water smelt eye decreased approximately 3 orders of magnitude, which is once again consistent with what's found in the literature.

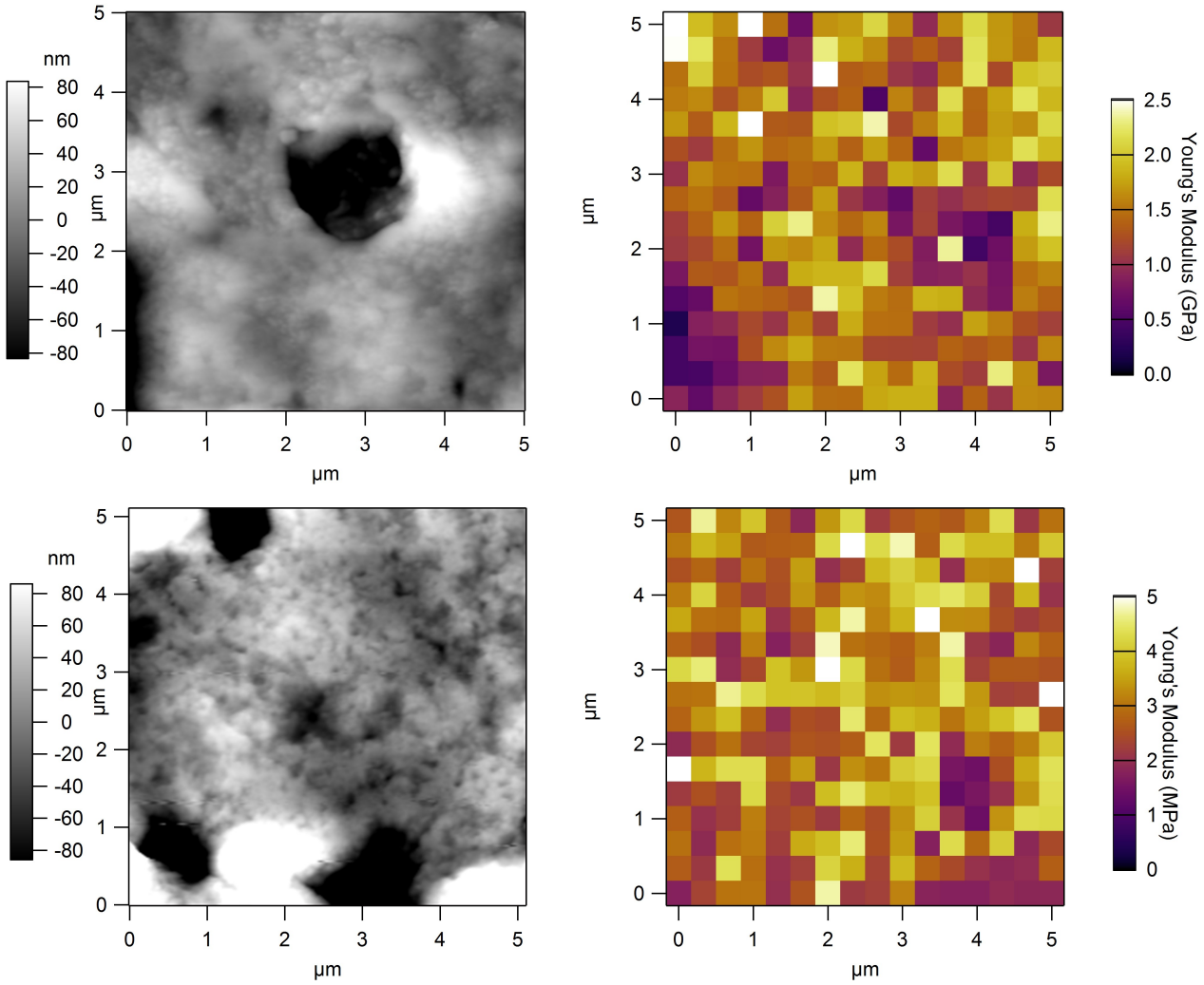

Figure 3.6: Highlighting the topography and Force maps of the cold water rainbow smelt eye tissue. Top left: height image of the dry eye tissue, with its corresponding force map (top right). Bottom left: height image of the hydrated eye tissue, with its corresponding force map (bottom right)

Table 3.5: Comparison of the average Young's modulus values of the dry and hydrated *cold water* smelt eye tissue (N=3)

	Average Young's Modulus (MPa)	Standard Deviation (MPa)	Statistically Different? (P value)
Dry	1426.6	469.9	**YES** (P=9 $\times 10^{-131}$)
Hydrated	3.065	0.96	

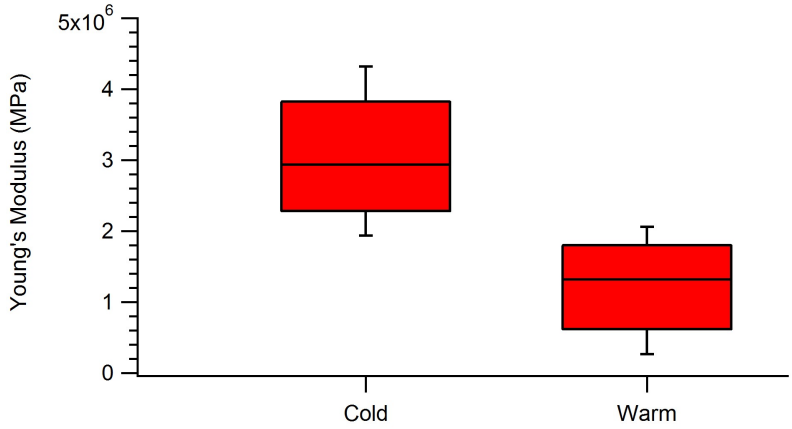

Figure 3.7: Box plot showing the difference in average Young's Modulus values of the hydrated cold and warm water smelt eye tissue. Data taken from Tables 3.4 and 3.5

The 2-3 order of magnitude decrease in Young's modulus seen in biological materials upon hydration, including the smelt eyes samples studied, can be attributed to the effect that hydration has on the proteins and lipid membranes in the tissue. Based on the large decrease in Young's modulus seen from hydrating the sample with ultrapure water, the mechanical properties of the eye tissue must be heavily influenced by the liquid phase of the material. One such theory behind the decrease in Young's modulus was proposed by Grant *et. al* in a previous paper. In this paper, Grant attributes the decrease in Young's modulus of hydrated collagen fibrils to the formation of water bridges between peptide chains in the protein [78, 79]. These water bridges occur between oxygen atoms within a single peptide, between two peptide chains, or between multiple collagen triple helices, and serves to stabilize the proteins

through a network of hydrogen bonding. The same bridging effect can be seen in lipid membranes, where water molecules stabilize the membrane through water bridging of lipid molecules [80]. The decrease in Young's modulus seen upon hydration of the smelt eye tissues can be attributed to the stabilizing effect the water molecules has on both the proteins and lipid membranes present in the sample.

As previously discussed in Section 2.3.2, the Young's modulus of the dry cold water smelt eye tissue was found to be higher than that of warm water eye. The results from force mapping experiments of the same eye samples in a hydrated environment are highlighted in Figure 3.7. Upon hydrating the samples, the tissue in the vascular region of the eye has a higher Young's modulus in the cold water fish over the warm water. This is the same result as seen with the dry eye samples discussed in Chapter 2. This result implies that the reason behind the difference in Young's modulus between the two eyes is independent of whether or not the sample is hydrated. As such, the possible explanations for the difference in Young's modulus outlined in Chapter 2.3.2 still hold true, even in a hydrated environment.

3.3.3 The Effect of Ionic Strength on Young's Modulus

As mentioned in Section 3.1, previous work performed by C. Grant *et. al* showed that the apparent Young's modulus of collagen fibrils in fluid is influenced by the ionic environment of the hydrating solution. Up to now, in-fluid analysis of the eye cross sections has been performed primarily in ultrapure water in an attempt to better replicate the biological environment. However, a more realistic model would include other ions which are prominent within the eye such as potassium [81] and sodium [82]. In attempt to better model the eye, aliquots of sodium chloride solution was added to the AFM setup in order to increase the ionic strength of the environment. Force mapping at different ionic strengths was then performed to see if any change in average

Young's modulus can be seen.

The ionic strength experiment were performed on the warm water smelt eye sample. The average Young's modulus values determined from the force mapping experiments are outlined in Table 3.6 and Figure 3.8. When only ultrapure water is used to hydrate the sample, the average Young's modulus was determined to be 1.820 ± 0.75 MPa, which is similar to the average Young's modulus determined in Section 3.3.2. With the first addition of NaCl achieving an ionic strength of 0.499 mol/L, the average Young's modulus of the cold eye sample increased to 2.503 ± 0.78 MPa, and increased once again to 3.021 ± 1.00 MPa when the ionic strength of the fluid in the AFM experiment was increased to 0.666 mol/L. Student's t-Tests confirmed that the average Young's modulus at each of these ionic strengths were statistically different from each other. Upon increasing the ionic strength of the AFM hydrating fluid to 0.798 mol/L, no statistically significant increase in average Young's modulus of the eye sample was seen.

Table 3.6: Average Young's modulus of the warm water smelt eye in differing ionic strength environments (N=12)

Ionic Strength of Solution (mol/L)	Average Young's Modulus (MPa)	Standard Deviation (MPa)
0	1.820	0.75
0.499	2.503	0.78
0.666	3.201	1.00
0.798	2.976	1.06

The increase in Young's modulus seen with increasing ionic strength of the hydration environment is similar to what was reported in Grant *et. al.* The observed increase in Young's modulus can be attributed to slight changes in the intermolecular interactions between proteins present in the eye [77, 83]. In particular, alterations in the electronic environment caused by the changes in ionic strength can lead to increased stability of proteins as seen in the paper published by Atkaş [84]. In this

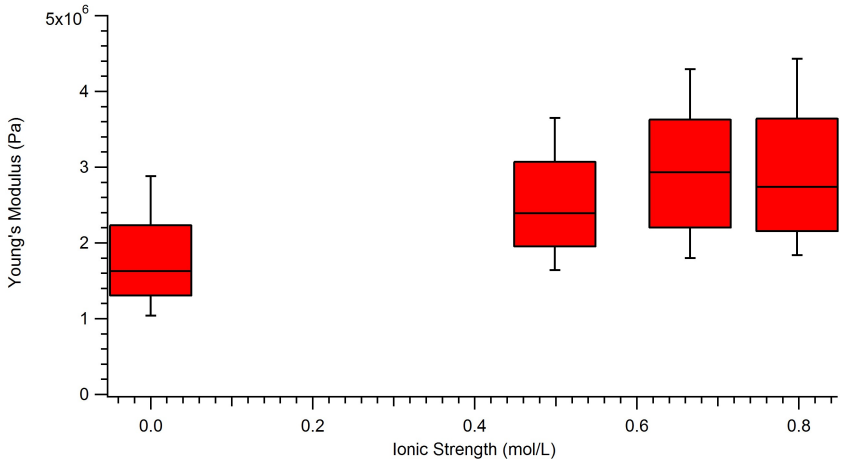

Figure 3.8: Box plot showing the relationship between the ionic strength of the hydrating solution used during the force mapping experiment and the average Young's modulus of the warm water smelt eye sample. Data taken from Table 3.6

study, the addition of NaCl to a solution of collagen proteins resulted in an increase in thermal stability over proteins in a citrate buffer. The increase in thermal stability is caused by the reduced net repulsion between the proteins, as Na^+ and Cl^- ions bind to charged residues in the protein, and can also act as ionic crosslinkers between charged residues of the protein [85]. Furthermore, the presence of NaCl results in an increase in the polypeptide-chain rigidity of the collagen. This results in a protein structure which becomes more rigid through electrostatic interactions with ions introduced when increasing the solution ionic strength. Increasing the ionic interactions within a protein or phospholipid network has been shown to increase its Young's modulus as the structure becomes more rigid, or less fluid in the case of phosopholipids [86, 87]. Increasing the NaCl concentration of the smelt eye environment will result in the same changes in protein and phospholipid structure, hence the observed increase in the apparent Young's modulus of the eye.

3.4 Conclusions

Hydration of the rainbow smelt eye tissues resulted in vast changes in both their morphological and mechanical properties. Hydrating both the cold and warm water smelt eye samples resulted in a swelling of the eyes caused by water entering the tissues through osmotic force. Both the cold and warm eyes swelled to 1.5 and 1.6 times their size, respectfully, compared to their dried states. This degree of tissue swelling is comparable to what has been found in the literature. Despite the swelling caused by hydration, the same porous topography was observed in the vascular region of the eye compared to that found in the dried eye samples. Hydration also resulted in an approximate 3 orders of magnitude decrease in the Young's modulus, which can be attributed to changes in protein and membrane environments upon introducing water. We once again see that the cold water smelt eye tissue has a higher average Young's modulus than the warm water eye tissue, indicating that the possible reason behind this difference outlined in Chapter 2 is not influenced by whether the tissue is dry or hydrated. Upon increasing the ionic strength of the hydrating fluid with NaCl, the warm water smelt eye tissue saw an increase in average Young's modulus. This increase can be attributed to the added ions in solution acting as ionic crosslinks between protein and phospholipids, causing stabilization and increasing rigidity in the eye tissues.

Chapter 4

Conclusions and Future Work

4.1 Concluding Remarks

In this research, we studied the morphological and mechanical properties of eye tissue of the Rainbow smelt (*Osmerus mordax*) using atomic force microscopy. Specifically, we compared these properties between two sub-sets of smelts: fish which were raised in water of ambient temperatures, and fish which were raised in a cold-water temperature environment. Our analysis focused on a porous area of tissue near the back area of the eye samples, which we proposed was either the retina or choriocapillaris due to the high density of blood vessels in these microstructures. Upon comparing the morphologies of this vascular region of the eye, no noticeable differences were seen between the two fish eye subsets. Analysis of the pore depth between the two subsets of smelt eyes was also performed, but no statistical difference between the pore sizes. However, upon analysis of the mechanical properties of the smelt eyes, we discovered that the average Young's modulus of the smelt eye raised in the cold water environment was higher than that of the smelt raised in the ambient, warm water environment, indicating that the tissue in the cold water smelt eye is stiffer than its warm water counterpart.

While the reason behind this difference is currently unknown, we suspect that this may be caused by the osmolytes (glycerol, urea) or antifreeze proteins present in the fish which help acclimatize the cold water fish to its environment. [19] Another reason behind the increase in Young's modulus seen in the cold water fish tissue involves lipid membrane restructuring, a phenomena commonly seen in cold water ectotherms. [72] The degree of unsaturated fatty acids in lipid membranes increases in colder environments to help promote lipid peroxidation, which is required for some cellular processes to occur. These changes in chemical or lipid composition of the tissue may be the cause of the stiffening of the cold water smelt eye tissue we have observed in this work.

The effects of hydration on the smelt eye samples was also studied using atomic force microscopy. Hydration of the smelt eye resulted in a swelling of the tissues, which is driven by osmotic forces caused by a solute concentration gradient between cell interior and the outside water environment. Hydration resulted in a 1.5-1.6 times increase in tissue size, for the cold water and warm water vascular eye tissue respectively, which is similar to the increase in size of other biological materials upon hydration. [77] This hydration also resulted in a near 3 orders of magnitude decrease in Young's modulus compared to that found in the dry samples, as reintroducing water to the tissues results alterations to the bonding environment of the proteins and lipids present, including the formations of water bridges [78, 79], which causes a decrease in Young's modulus. However, the cold water smelt eye tissue is still stiffer than the warm water tissue in the hydrated environment, indicating that the reason behind the difference in Young's modulus between the two is not influenced by whether the tissue is hydrated or not. We also discovered that increasing the ionic strength of the hydrating solution causes the eye tissue to increase in Young's modulus, as additional ions present in solution alter the electrostatic environment in the eye tissue. Added

stability through ionic cross-linking between lipids or proteins increases the rigidity of the tissues. [85]

4.2 Future Work

While this work contains a solid foundation on analysis of these rainbow smelt eye tissues, there are many more questions which need to be answered to help gain a clearer picture behind the results we have found.

First and foremost, gaining an understanding as to why there is an increase in Young's modulus of the eye tissue in cold water rainbow smelt is critical. Outlined in Section 2.3.2 were two possible theories behind the observed difference in Young's moduli: the presence of osmolytes such as glycerol and urea in the tissue, or lipid membrane reconstruction. To determine whether the osmolytes have influence on the Young's modulus, Tip-Enhanced Raman Spectroscopy (TERS) mapping of the samples could be performed. TERS is a technique which combines the spectroscopic information obtained during Raman spectroscopy experiments with the topographical information gathered during AFM imaging [88]. TERS has been highly used in the chemical exploration of biological materials, and has been used to perform such experiments as DNA sequence and amino acid determination of samples [89, 90].

Using TERS in the analysis of the smelt eye samples would provide us with simultaneous structural and chemical information of the tissues. As such experiments allow for the mapping of the intensity specific Raman shifts, this allows us to map out specific Raman shift values we would expect to see in our osmolytes of interest. As such, we could map the intensity of the C-OH stretch seen in glycerol (1049 cm^{-1}) [91], NH_2 stretch of urea (3450 cm^{-1}) [92], and the sulfur-sulfur stretch (499 cm^{-1}) and carbon-sulfur (678 cm^{-1}) of the cysteine-rich antifreeze proteins [93] across the topog-

raphy of the smelt eye samples. Following the chemical mapping, force mapping of the same area can be performed to determine if areas with higher amounts of osmolytes correlate to areas of the eye with a larger, or smaller Young's modulus values.

To determine if the change in Young's modulus is caused by lipid membrane reconstruction, the composition of the lipids present in both the warm and cold water smelt eye tissues would need to be determined. Digesting the eye samples, and performing liquid chromatography (LC) with electrospray ionization mass spectrometry (ESI/MS) can be used to separate and quantify the phospholipids present in the eye tissues [94]. By doing this, we can determine if there is a difference in unsaturated fatty acids content of the cold and warm water smelt eye tissues, which could give a better understanding as to whether it relates to the observed difference in Young's modulus of the cold and warm water samples.

Furthermore, the scope of this work has focused solely on one property of the eye tissues, that being the Young's modulus. While many models which are used to determine Young's modulus assume that the samples are linearly elastic in nature [50], biological materials are known to have considerable viscoelastic properties [52, 95]. Studies into the viscoelastic properties of both the cold and warm water smelt eye tissues, such as a creep experiment, would be ideal in continuing to understand more about the physical properties of these biological samples [96].

Appendix A

The Production of Tip-Enhanced Raman Spectroscopy (TERS) Tips

A.1 Introduction

The use of Tip-Enhanced Raman Spectroscopy (TERS) for chemical analysis of samples relies on a precise and reliable method of producing tips [97]. In theory, the ideal tip is made of a conductive metal such as gold or silver, and its apex radius is as small as possible to produce the highest resolution data. While commercial tips are available for purchase, many groups opt for in-house production of their own tips. This appendix will outline the several different methods for TERS tip production attempted throughout my masters program.

A.2 Experimental

A.2.1 Etching in HCl/Methanol Solution

This method is based off of the published procedure of Ren *et. al.* [97] Approximately 5 mL of a 50/50 solution of HCl:methanol (Fisher Scientific) is pipetted into a 10 mL beaker placed in a fumehood. Using gold wire (Aldrich), a gold ring is made that can be hung from the side of the beaker as seen in Figure A.1. The gold ring sits on the surface of the 50:50 HCl:MeOH solution, where a strand of gold wire (Aldrich) is immersed into the solution through the centre of the gold ring. Both the gold ring and immersed gold wire are attached to a potentiostat via alligator clips. A direct current (DC) voltage of 2.5 V is applied to the system, initiating the electrochemical etching of the gold wire in the solution. When the gold wire has etched to the surface of the solution, the current in the electrochemical cell is broken and the DC voltage drops to zero. The etched gold wire is removed from the set up and gently rinsed with 18.2 MΩ·cm ultrapure water (hereafter referred to as ultrapure water).

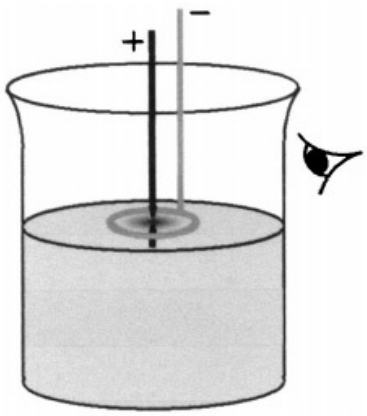

Figure A.1: General schematic outlining the setup used to produce TERS tips in Section A.2.1 [97]

A.2.2 Etching in H_2SO_4 Solution

This method is based off the published procedure of Hodgson *et. al.* [98] Approximately 5 mL of concentrated H_2SO_4 (Fisher) was pipetted into a 10 mL beaker placed in a fumehood. The setup for this experiment was identical to that shown in Figure A.1. A direct current (DC) voltate of 6.5 V was applied to the system. When the gold wire has etched to the surface of the solution, the current in the electrochemical cell is broken and the DC voltage drops to zero. The etched gold wire is removed from the set up and gently rinsed with ultrapure water.

A.2.3 Etching in NaCl/$HClO_4$ Solution

This method is based off the published procedure of Gingery *et. al.* [99] 3.0 M NaCl in 1 % $HClO_4$ was used as an etchant solution. 5 mL of the etchant solution was pipetted into a 10 mL beaker placed in a fumehood where a portion of gold wire (Aldrich) was submerged into the solution. A graphite rod was removed from a number two pencil for use as the counterelectrode in this experiment, which was also placed in the etchant solution. The wire and counterelectrode are connected to a potentiostat via aligator clips in the same manner as outlined in Section A.2.1. A DC voltage of approximately 2.5 V was applied, causing the etching of the gold wire. The current in the system breaks when the gold wire etches to the surface of the solution, indicating completion. The etched gold wire is removed from the set up and gently rinsed with ultrapure water.

A.2.4 Etching in a $CaCl_2$ Droplet

This method is based on the published procedure of Snitka *et. al.* [100] First, a portion of gold wire (Aldrich) was fixed to the back of a AFM chip with broken tips (Mikromasch) using nailpolish, resulting in a probe which will look very similar to a typical AFM tip setup as shown in Figure A.2. A 30 μL drop of 50/50 saturated $CaCl_2$/ultrapure water solution was deposited on a sheet of aluminum foil using a micropipette. A portion of gold wire was placed in the droplet. Alligator clips were used to connect the gold wire and aluminum foil to a potentiostat. A DC voltage of 10 V was applied to etch the gold wire, and continued until the circuit broke due to the evaporation of the etchant solution. The etched gold wire was then rinsed with ultrapure water.

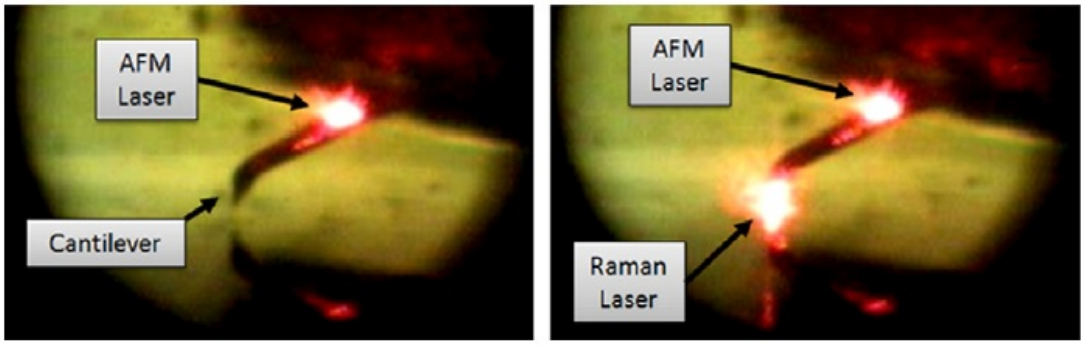

Figure A.2: Gold wire etched by $CaCl_2$ glued to the back of a typical AFM chip, resulting in a TERS probe which is very similar to an AFM tip [100]

A.2.5 Silver-Coated SiN AFM Probes

In this process, a thin layer of silver metal is deposited onto a standard AFM tip, which is then used as a TERS probe using the standard AFM tapping mode feedback loop outlined in Chapter 1.2.2. The process of metal deposition was previously described in L. Whelan's Masters thesis [101]. In summary, top-visual silicon tapping mode

AFM tips (VIT_P series, NT-MDT) were placed on a strip of polydimethylsiloxane (PDMS) taped to a glass slide. The glass slides were placed on a sample holder which allows the samples to be held above the metal evaporation source in a house-built metal evaporation system. A quartz crystal microbalance (INFICON XTM/2 deposition monitor) is used to monitor the thickness of the metal deposition on the substrate. Silver shots (Alfa Aesar, 1-5 mm, 99.9 % metal basis purity) were placed in a tungsten boat in the evaporation chamber. Metal deposition was used to deposit a film of silver with thickness of 40 nm as monitored by the quartz crystal microbalance, resulting in a TERS probe with a tip radius of approximately 50 nm.

A.2.6 Gold-Coated SiN AFM Probes

Preparation of the gold-coated AFM probes followes the same procedure as outlined in the preparation of silver-coated probes in Section A.2.5. top-visual silicon tapping mode AFM tips (VIT_P series, NT-MDT) were placed on a strip of polydimethylsiloxane (PDMS) taped to a glass slide. The glass slides were placed on a sample holder which allows the samples to be held above the metal evaporation source in a house-built metal evaporation system. A quartz crystal microbalance (INFICON XTM/2 deposition monitor) is used to monitor the thickness of the metal deposition on the substrate. Gold wire (Alfa Aesar, 99.9 % metal basis purity) were placed in a tungsten wire basket in the evaporation chamber. Metal evaporation was used to deposit a film of gold with thickness of 10 nm as monitored by the quartz crystal microbalance, resulting in a TERS probe with a tip radius of approximately 20 nm.

A.3 Results and Discussions

The TERS probe serves a dual purpose in a typical TERS experiment. First, it must act as a scanning probe microscopy tip in order to provide topographic information of the surface being scanned. In this regard, metal-coated AFM probes pose a huge advantage over etched wires due to their ease of use. The same feedback loops and setup which are normally employed during tapping mode AFM imaging can be used during the TERS experiment to collect the topographic information about the sample. The other purpose of the TERS probe is to provide enhancement of the Raman signal near the apex of the tip [102]. Hence, the ability for a probe to create this signal enhancement is the true test as to whether or not it will work during an experiment.

To test the effectiveness of the TERS probes produced, the probes were loaded onto tip holders to be used in the AFM (NTEGRA Spectra, NT-MDT). Gold and silver-coated AFM probes were loaded into the stock AFM probe holder which was then placed in to the AFM head. TERS probes made from etched gold wire were adhered to a tuning fork (TF 103_NFT, NT-MDT), placed in a tuning fork probe holder, and then placed in the AFM head. The tip was brought close to the sample surface, and the Raman laser (633 nm) was positioned near the tip of the TERS probe. A series of Raman spectra were taken of the area around the tip apex in attempt to locate the Raman hot spot. The ability for the TERS probe to produce a Raman hot spot is the ultimate indication of whether or not the probe will work in a TERS experiment. Unfortunately, for all the probes we made for the TERS trial experiments failed to produce a Raman hot spot, meaning they could not be used to perform TERS mapping experiments. The issue of being able to make reliable and reproducible TERS probes is still an issue within the field of research [103]. There currently stands no proven method to produce reliable TERS probes that are guaranteed to work, making its use within the lab extremely challenging [104]. However, as the method develops and

more researchers aim towards developing standard protocols towards these methods, producing reliable TERS tips will become much simpler.

Appendix B

Performing Atomic Force Microscopy Imaging in Fluid

B.1 Introduction

Performing Atomic Force Microscopy (AFM) in fluid is highly advantageous over typical ambient imaging when studying biological materials, as discussed in Section 3.1. This appendix will outline the standard method of calibrating, introducing fluid, and imaging used in my experiments, which can serve as the standard method for performing in-fluid imaging of materials using AFM.

B.2 Experimental

B.2.1 Initial Setup

An atomic force microscope (MFP-3D, Asylum Research) is used to perform the in-fluid imaging of all samples. Load a gold-chromium coated AFM probe (HQ:CSC37/Cr-Au, Mikromasch) with a spring constant of approximately 0.4 N/m in to the AFM tip

holder, and then placed into the AFM head. Align the laser on the back of one of the AFM cantilevers and maximize the laser sum signal, and then set the laser deflection value to -1 V. Ensure the AFM head is properly levelled.

B.2.2 Calibration of the Tip (In Air)

Calibration the AFM tips inverse optical lever sensitivity (invOLS) is based on the procedure outlined in Reference 63. In short, perform a force-distance curve on a hard surface such as a Si wafer or freshly cleaved mica. From the resulting force-distance curve, highlight the approach phase of the curve, and place markers on at two points along the flat, horizontal portion of the trace. Under the force tab of the master panel, select the 'cal' sub tab. Under the 'Set-sens' pull down menu, select 'virtual defl line'. This will set the virtual deflection value of your force curve, in such that this free-air portion of the curve where the tip is moving towards your surface will have a constant deflection value. Next, perform another force-distance curve just like above. Highlight the indentation portion of the force-distance curve, and place markers on the indentation portion of either the approach or retract phase. From the same 'Set-sens' pull down menu, select 'Defl invOLS'. This will set the invOLS value for the calibration force-distance curve. This value is necessary in determining the proper spring constant of the tip. Next, disengage the tip from the surface, and raise the AFM head to remove the tip from the sample, and set the laser deflection value to 0 V. Next, perform a thermal calibration of the tip, in-air, to determine the spring constant of the tip. If at this point the spring constant of the tip is outside of the factory-provided specs, replace the tip with a new one and re-perform the calibration process.

B.2.3 Introducing Fluid to the Setup

Reset the laser deflection value to -1 V and lower the tip to the surface until in contact. When in contact, bring the AFM head up slightly again as to bring the tip back out of contact. Using a micropipette, place the pipette tip near the AFM tip and sample, and dispense approximately 25 to 50 μL of ultrapure water. If done properly, the water should wick upwards and encompass both the AFM tip and the sample. Let the setup equilibrate for approximately 15 minutes. Once equilibrated, the sum signal and laser deflection values may need to be readjusted.

B.2.4 Re-calibration and Tuning of the Tip (In Fluid)

Once the AFM tip is in fluid, recalibration is required. First, the tip invOLS will need to be performed again, in the same manner as outlined in Section B.2.2. Once completed, the AFM mode needs to be changed to 'AcAir' (also known as tapping mode), and can be done on the main tab of the master panel. Set the laser deflection value to 0 V, and ensure the set point is at 800 mV. Tune the tip by entering the 'Tune' tab on the master panel. Perform a continuous tune of the tip at the resonant frequency determined by the thermal tune during the invOLS calibration. If a resonant frequency is not obvious upon beginning the continuous tune, restart the tune using a slightly higher frequency range. Upon finding the resonance frequency of the tip, right-click on the peak using the AFM software, slightly to the left of the maximum, and select 'Set Drive Frequency'. Right click again and select 'Centre Phase'. Next, begin increasing the drive frequency of the tip to increase the amplitude of the resonance frequency to a value that is greater than your initial set point of 800 mV. Aiming for a drive amplitude of near or slightly above 1.0 V works well. When completed, save your tuning plots, and begin imaging using standard tapping mode.

B.3 Results and Discussion

Following the above method, one should be able to image hydrated biological samples using tapping mode AFM techniques. If the method above is followed and does not produce an image during AFM scanning, repeating the calibration process in Section B.2.4 is advisable. Otherwise, this method has proven sound for the AFM imaging of samples in fluid.

Bibliography

[1] A. L. Lehninger, D. L. Nelson, and M. M. Cox. *Principles of Biochemistry*. Worth Publishers: New York NY, 2nd ed. edition, 1993.

[2] N. Demaurex. *News in Physiological Sciences*, 17(1):1–5, 2002.

[3] Y. Hiraoka, T. Matsuoka, M. Ohno, et al. *Nature Communications*, 5:1–11, 2014.

[4] S. Baldassano, F. Rappa, A. Amato, et al. *Journal of Cellular Physiology*, 230:3029–3036, 2015.

[5] A. Southon, R. Burke, M. Norgate, et al. *Biochemical Journal*, 383:303–309, 2004.

[6] C. Waymouth. *In Vitro*, 6(2):109–127, 1970.

[7] C. Brocker, D. Thompson, and V. Vasiliou. *Biomolecular Concepts*, 3(4):345–364, 2012.

[8] A. D. Association. *Diabetes Care*, 36(Supplement 1):S67–S74, 2013.

[9] L. Guariguata, D. Whiting, I. Hambleton, et al. *Diabetes Research and Clinical Practice*, 103:137–149, 2014.

[10] M. Campbell-Thompson, T. Rodriguez-Calvo, and M. Battagila. *Current Diabetes Reports*, 15(10):1–6, 2015.

[11] D. Do, X. Wang, S. Vedula, et al. *Cochrane Database of Systematic Reviews*, (1):1–114, 2015.

[12] F. Willermain, S. Libert, E. Motulsky, et al. *Frontiers in Physiology*, 5:1–8, 2014.

[13] T. Cuilla, A. Amador, and B. Zinman. *Diabetes Care*, 26(9):2653–2664, 2003.

[14] P. Calvo, B. Abadia, A. Ferreras, et al. *Drugs*, 75(13):1461–1469, 2015.

[15] M. Larsen. *Acta Ophthalmologica Scandinavica*, 83(4):428–435, 2005.

[16] J. Zhou, S. Wang, and X. Xia. *Current Eye Research*, 37(5):416–420, 2012.

[17] J. Treberg, C. Wilson, R. Richards, et al. *Journal of Experimental Biology*, 205(10):1419–1427, 2002.

[18] H. Levesque, C. short, T. Moon, et al. *Canadian Journal of Fisheries & Aquatic Sciences*, 62:2854–2863, 2005.

[19] R. Gendron, E. Armstrong, H. Paradis, et al. *Molecular Vision*, 17:2596–2604, 2011.

[20] R. García and R. Pérez. *Surface Science Reports*, 47:197–301, 2002.

[21] J. Alonso and W. Goldmann. *Life Sciences*, 72(23):2553–2560, 2003.

[22] S. Belaidi, P. Girard, and G. Levesque. *Journal of Applied Physics*, 81:1023–1030, 1997.

[23] U. Hartmann. *Physical Review B*, 43(3):2404–2407, 1991.

[24] G. Binnig, C. Quate, and C. Gerber. *Physical Review Letters*, 56(9):930–933, 1986.

[25] H. Butt, B. Cappella, and M. Kappl. *Surface Science Reports*, 59:1–152, 2005.

[26] E. Meyer. *Progress in Surface Science*, 41:3–49, 1992.

[27] M. Chyasnavichyus, S. Young, and V. Tsukruk. *Japanese Journal of Applied Physics*, 54:08LA02 1–08LA02 13, 2015.

[28] Q. Zhong, D. Inniss, K. Kjoller, and V. Elings. *Surface Science Letters*, 290(1-2):L688–L692, 1992.

[29] R. García and A. Paulo. *Physical Review B*, 60(7):4961–4967, 1991.

[30] Y. Efremov, P. E, and K. Shaitan. *Micron*, 42:840–852, 2011.

[31] M. Pfreundschuh, D. Martinez-Martin, E. Mulvihill, et al. *Nature Protocols*, 9(5):1113–1130, 2014.

[32] A. Tavakolinejad, M. Rabbani, and M. Janmaleki. *Biochemical and Biophysical Research Communications*, 464:473–479, 2015.

[33] J. Dias, V. Diakonis, M. Lorenzo, et al. *Experimental Eye Research*, 138:1–5, 2015.

[34] A. Baró and R. Reifenberger. *Atomic Force Microscopy in Liquid: Biological Applications*. John Wiley & Sons: Weinheim Germany, 1st ed. edition, 2012.

[35] J. Sader. *Journal of Applied Physics*, 84:64–76, 1998.

[36] S. Basak and A. Raman. *Applied Physics Letters*, 91:06417 1–06417 3, 2007.

[37] A. Janshoff, M. Meitzert, Y. Oberdörfer, and H. Fuchs. *Angewandte Chemie International Edition*, 39:3212–3237, 2000.

[38] V. Morris, A. Kirby, and A. Gunning. *Atomic Force Microscopy for Biologists*. Imperial College Press: London, UK, 2nd ed. edition, 2010.

[39] H. Jin, H. Zhao, et al. *Molecular Biology Reports*, 38(7):4495–4500, 2011.

[40] B. Cappella and G. Dietler. *Surface Science Reports*, 34:1–104, 1999.

[41] B. Cappella and W. Stark. *Journal of Colloid and Interface Science*, 296:507–514, 2006.

[42] G. Tronci, C. Grant, N. Thomson, et al. *Interface*, 12:1–13, 2014.

[43] N. Nijenhuis, X. Zhao, A. Carisey, et al. *Biophysical Journal*, 107:1502–1512, 2014.

[44] Q. Li, G. Lee, C. Ong, and C. Lim. *Biochemical and Biophysical Research Communications*, 374:609–613, 2008.

[45] D. Askeland, P. Fulay, and W. Wright. *The Science and Engineering of Materials*. Global Engineering: Stamford, CT, 6th ed. edition, 2011.

[46] J. Hay and P. Wolff. *Journal of Materials Research*, 16(5):1280–1286, 2001.

[47] Y. Chen, C. Qian, and N. Miao. *Thin Solid Films*, 579:57–63, 2015.

[48] P. Mott and C. Roland. *Physical Reviews B*, 80:132104:1–132104:4, 2009.

[49] S. Park and Y. Lee. *International Journal of Biological Sciences*, 9(7):702–706, 2013.

[50] Y. Chang, V. Raghunathan, S. Garland, et al. *Journal of the Mechanical Behaviour of Biomedical Materials*, 37:209–218, 2014.

[51] M. Murphy, F. Lilley, M. Lalor, et al. *Microscopy Research and Techniques*, 76:36–41, 2013.

[52] Y. Feng, E. Clayton, Y. Chang, et al. *Journal of Biomechanics*, 46(5):863–870, 2013.

[53] D. Lin, E. Dimitriadis, and F. Horkay. *Journal of Biomechanical Engineering*, 129:903–912, 2007.

[54] K. Johnson, K. Kendall, and A. Roberts. *Proceedings of the Royal Society A: Mathematical, Physical, and Engineering Sciences*, 324:301–313, 2013.

[55] D. Ebenstein. *Journal of Materials Research*, 26(8):1026–1035, 2011.

[56] C. Xu. *Nanostructure and Nanomechanics of Collagen Self-Assemblies*. PhD thesis, Memorial University of Newfoundland, 2014.

[57] M. Baclayon, G. Wuite, and W. Roos. *Soft Matter*, 6:5273–5285, 2010.

[58] S. Das, P. Sreeram, and A. Raychaudhuri. *Nanotechnology*, 18(3):1–6, 2007.

[59] H. Butt and M. Kappl. *Advances in Colloid and Interface Science*, 146:48–60, 2009.

[60] D. Macdonald. *Clinical and Experimental Optometry*, 97:311–323, 2014.

[61] W. Driedzic and K. Ewart. *Comparative Biochemistry and Physiology B: Biochemistry and Molecular Biology*, 139(3):347–357, 2004.

[62] J. Hutter and J. Bechhoefer. *Review of Scientific Instruments*, 64:1868–1873, 1993.

[63] R. Fuierer. *Asylum Research Procedural Operations Manualette*. Asylum Research.

[64] A. A. Alhasawi. Microstructural Imaging of the Eye and Mechanical Mapping of Retinal Tissue using Atomic Force Microscopy (AFM). Master's thesis, Memorial University of Newfoundland, 2016.

[65] H. Kolb. *WEBVISION: The Organization of the Reina and Visual System [Internet]*, pages 1–25, 2005.

[66] D. Henkind, R. Hansen, and J. Szalay. *Physiology of the Human Eye and Visual System*. Harper & Row: Hagerstown, MD, 1979.

[67] S. Ifuku, A. Ikuta, H. Izawa, et al. *Carbohydrate Polymers*, 101:714–717, 2014.

[68] A. Aguirre, R. Boreno, and A. León. *Industrial Crops and Products*, 50:297–303, 2013.

[69] S. Vijayan, R. Narasimman, and K. Prabhakaran. *Journal of the American Ceramic Society*, 96(9):2779–2784, 2013.

[70] K. Ewart and G. Fletcher. *Canadian Journal of Zoology*, 68(8):1652–1658, 1990.

[71] F. Galindo, D. Vaughan, W. Herppich, et al. *European Journal of Horticultural Science*, 69(6):229–234, 2004.

[72] E. Crockett. *Journal of Comparative Physiology B*, 178(7):795–809, 2008.

[73] W. Lin and C. Huang. *Comparitive Biochemistry and Physiology*, 144C:327–333, 2007.

[74] A. Lee. *Biochemica et Biophysica Acta - Biomembranes*, 1666(1-2):62–87, 2004.

[75] M. Stacey, D. Dutta, W. Cao, et al. *Micron*, 44:483–487, 2013.

[76] L. Yoo, J. Reed, A. Shin, et al. *Journal of Biomechanics*, 47(8):1899–1903, 2014.

[77] C. Grant, D. Brockwell, S. Radford, et al. *Biophysical Journal*, 97(11):2985–2992, 2009.

[78] C. Grant, D. Brockwell, S. Radford, et al. *Applied Physics Letters*, 92(23):2006–2009, 2008.

[79] J. Bella, B. Brodsky, and H. Berman. *Structure*, 3(9):893–906, 1995.

[80] E. Yamamoto, T. Akimoto, M. Yasui, and K. Yasuoko. *Scientific Reports*, 4(4720):1–7, 2014.

[81] K. Ferslew, A. Hagardorn, M. Harrison, et al. *Electrophoresis*, 19:6–10, 1998.

[82] H. Chandrakanth, T. Kanchan, B. Balaraj, et al. *Journal of Forensic and Legal Medicine*, 20(4):211–216, 2013.

[83] U. Freudenberg, S. Behrens, P. Welzel, et al. *Biophysical Journal*, 92:2108–2119, 2007.

[84] N. Atkaş. *Thermochimica Acta*, 407:105–112, 2003.

[85] J. Berger, M. Reist, J. Mayer, et al. *European Journal of Pharmaceutics and Biopharmaceutics*, 57:19–34, 2004.

[86] M. Guthwold, W. Liu, E. Sparks, et al. *Cell Biochemistry and Biophysics*, 49(3):165–181, 2007.

[87] X. Wang, R. Sanderson, and R. Ragan. *Journal of Biophysical Chemistry C*, 118:29301–29309, 2014.

[88] M. Ghislandi, G. Hoffmann, E. Tkayla, et al. *Applied Spectroscopy Reviews*, 7:371–381, 2012.

[89] R. Treffer, X. Lin, E. Bailo, et al. *Belistein Journal of Nanotechnology*, 2:628–637, 2011.

[90] D. Kurouski, T. Deckert-Gaudig, V. Deckert, and I. Lednev. *Biophysical Journal*, 106:263–271, 2014.

[91] A. Mudalige and J. Pemberton. *Vibrational Spectroscopy*, 45:27–35, 2007.

[92] R. Keuleers, H. Desseyn, B. Rousseau, and C. Alsenoy. *Journal of Physical Chemistry A*, 103(24):4621–4630, 1999.

[93] G. Zhu, X. Zhu, Q. Fan, and X. Wan. *Spectrochimica Acta Part A: Molecular and Biomolecular Spectroscopy*, 78(3):1187–1195, 2011.

[94] J. Rozsypal, V. Koštál, P. Berková, et al. *Journal of Thermal Biology*, 54(SI):20–29, 2015.

[95] W. Serem, C. Bett, J. Ngunjiri, and J. Garno. *Microscopy Research and Technique*, 74(7):699–708, 2011.

[96] K. Yamaguchi, A. Thomas, and J. Busfield. *International Journal of Non-Linear Mechanics*, 68:66–70, 2015.

[97] B. Rin. *Review of Scientific Instruments*, 75(4):837–841, 2004.

[98] P. Hodgson, Y. Wang, A. Mohammad, et al. *The Review of Scientific Instruments*, 84(2):026109 1–026109 3, 2013.

[99] D. Gingery and P. Bühlmann. *The Review of Scientific Instruments*, 78:113703 1–113703 4, 2013.

[100] V. Snitka, R. Rodrigues, and V. Lendraitis. *Microelectronic Engineering*, 88(8):2759–2762, 2011.

[101] L. Whelan. Determining the Electronic Properties of Surface Enhanced Raman Spectroscopy Substrates. Master's thesis, Memorial University of Newfoundland, 2015.

[102] T. Schmid, L. Opilik, C. Blum, and R. Zenobi. *Angewandte Chemie*, 52:5940–5954, 2013.

[103] Y. Yang, Z. Li, M. Nogami, et al. *RSC Advances*, 4(9):4718–4722, 2014.

[104] J. Stadler, T. Schmid, and R. Zenobi. *Nanoscale*, 4:1856–1870, 2012.